# MODELING AND SIMULATION OF BRAGG GRATINGS

# BY COMPLEX MODE MATCHING METHOD

# MODELING AND SIMULATION OF BRAGG GRATINGS ON HIGH INDEX CONTRAST AND SURFACE PLASMONIC WAVEGUIDES BY MODE MATCHING METHOD

By

JIANWEI MU, B.E.

A Thesis

Submitted to the School of Graduate Studies

in Partial Fulfillment of the Requirements

for the Degree

Master of Applied Science

McMaster University

MASTER OF APPLIED SCIENCE (2007) McMaster University

(Electrical and Computer Engineering) Hamilton, Ontario

TITLE: Modeling and Simulation of Bragg Gratings on High Index Contrast and Surface Plasmonic Waveguides by Mode Matching Method

AUTHOR: Jianwei Mu, B.E. (National University of Defense Technology, China)

SUPERVISOR: Professor Wei-ping Huang

NUMBER OF PAGES: xii, 55

# Abstract

As the fundamental basic building blocks of photonic circuits, optical waveguide structures play important roles in modern telecommunication and sensing systems. Various structures ranging from the dielectric waveguide utilizing the total internal reflection (TIR) to the more advanced structures based on the surface plasmon polaritions (SPPs) are widely investigated and studied in industrial and research areas. With the fast development of fabrication technologies, more and more complicated structures are predicated to emerge as the requirement of highly integrated photonic circuits. Modeling and simulation methods, as efficient as well as excellent cost performance tools comparing to costly facilities and time-consuming fabrication procedures, are demanded to explore and design the devices and circuits before their finalization.

This thesis reports a series of techniques to model two dimensional waveguide structures, including the conventional planar and surface plasmon polariton waveguides. This thesis contains both the methods and their applications to model and investigate the mode and propagation characteristics including the guided waves and the radiative waves. The methods include mode solvers based on finite difference method (FDM) and complex mode matching method (CMMM) , furnished with perfect matching layer (PML) for both guided and radiation modes. Based on the developed techniques, solutions of design of Bragg gratings with deep corrugations are presented; also various surface plasmon polariton (SPPS) grating structures are investigated.

# Acknowledgements

I would like to express my sincere gratitude to my supervisor, Dr. Wei-ping Huang, for his guidance, inspiration and discussions, in particular, for his great encouragement and understanding in various aspects throughout the entire process of this work. I would also like to express my great gratitude to Dr. Xun Li for his constructive suggestions and enlightening discussions. I am also grateful to Dr. Shiva Kumar, Dr. Chang-Qing Xu, Dr. Chih-Huang (James) Chen for their excellent course lectures.

So many thanks to Cheryl Gies, Helen Jachna and Jill Wood at Department of Electrical and Computer Engineering for their kindly help.

I am grateful to all of my colleagues, Hua Zhang, Min-hui (Steve) Yan, Qingyi Guo, Lei Zhao, Kai Jiang, Yu Chen, Yanping Xi, Kan He, Ranjbaran Mehdi, and Bin Xu, for their useful discussions.

I would like to express my deepest appreciation to my wife, my parents, and my sister and brothers for their support, believe and love.

# Contents

# List of Figures

# List of Tables

# Chapter 1
# Introduction

## 1.1 Background

In response to the needs of miniaturization and fast increased functionality in future integrated photonic chips, high contrast index waveguide structures are highly desired because the confinement of the traditional dielectric waveguides based on total internal reflection (TIR) is largely determined by the index contrast between waveguide core and cladding [1].

One the other hand, surface plasmon-polaritons (SPP) attracted much interests due to their unique properties characterized by large electromagnetic fields confined within a sub-wavelength region [2]. It has recently been shown a thin metal film surrounded by dielectric mediums can support two bound TM modes in which the symmetric mode has a very small attenuation constant, therefore the symmetric mode is often referred to as long range surface plasmon polaritons (LR-SPPs) mode and can be utilized to constitute low loss photonic components [3].

Periodic structures with index corrugations along optical waveguides are widely used in optical fiber and integrated optic devices and circuits [4-6]. Contra-propagating waves are coupled by the grating structures and the interference between the forward and the backward (guided or radiative) waves leads to a variety of spectral and spatial patterns.

The unique spectral and spatial characteristics of the Bragg gratings have been utilized in a wide range of applications such as wavelength filtering [7], input-output

coupling[8], optical feedback [9], sensing [10-12], etc. The long range surface plasmon polaritons Bragg grating has been investigated both theoretically and experimentally as a promising replacement of traditional dielectric gratings which are widely used in distributed feedback (DFB) and distributed Bragg reflector (DBR) lasers [2, 13-18].

## 1.2 Motivation

Different from the gratings based on the conventional weakly optical waveguides, the index contrast of the SPP structures or silicon on insulator waveguide is large and hence the vector nature of the fields is prominent. Especially only a limited number of methods were reported for modeling and simulation of SPP gratings so far, among which the finite-difference time-domain (FDTD) method is rigorous, yet extremely demanding on computation time and memory [19]. Other more efficient methods are the integral equations based on Green's functions and the mode matching method based on the guided surface mode[13, 20]. The mode-matching method based on single surface mode is intuitive and efficient, but lacks in accuracy, especially when the depth of the grating increases.

In this work, we employ a rigorous mode-matching method based on complex modes derived from a computation model facilitated by a perfectly matched layer (PML) terminated with zero boundary condition [21]. The complex modes including both the guided modes and the radiative leaky modes are computed by a highly accurate higher-order finite-difference solver [22].

## 1.3 Thesis organization

The arrangement of this thesis is as follows: In Chapter 2, the modal governing equations and finite difference solutions are presented. Chapter 3 describes the complex mode matching method. Simulation and analysis of deep gratings in dielectric waveguides with high index contrast are introduced in Chapter 4. Chapter 5 shows the analyses of the various SPPs gratings, and the conclusion of this thesis is drawn on Chapter 6.

# Chapter 2

# Mode Equations and Finite-Difference Solutions for Straight 2D Waveguides

## 2.1 Mode Equations for Straight 2D Waveguides

### 2.1.1 Governing equations for 2D waveguides

In a source-free, non-magnetic medium, the time-harmonic Maxwell's equations in their complex forms are written as

$$\nabla \times E = -j\omega\mu_0 H \tag{2.1}$$

$$\nabla \times H = j\omega\varepsilon_0\varepsilon_r E \tag{2.2}$$

$$\nabla \cdot (\varepsilon_0\varepsilon_r E) = 0 \tag{2.3}$$

$$\nabla \cdot (\mu_0 H) = 0 . \tag{2.4}$$

Where $\varepsilon_0$ and $\mu_0$ are the permittivity the permeability of the free space, $\varepsilon_r$ is the relative permittivity of the medium; A time harmonic factor $e^{j\omega t}$ is assumed and suppressed. The wave number $k_0$ and refractive index $n$ are defined as

$$k_0 = \frac{2\pi}{\lambda} \tag{2.5}$$

$$n = \sqrt{\varepsilon_r} . \tag{2.6}$$

By taking the curl of the (2.1) or (2.2) and substituting into the (2.2) or (2.1), we can eliminate one of the electric ( magnetic) fields to obtain the well known full vector wave equations:

$$\nabla\times[\nabla\times E]-\omega^2\mu_0\varepsilon_0 n^2 E=0 \tag{2.7}$$

$$\nabla\times\left[\frac{1}{n^2}\nabla\times H\right]-\omega^2\mu_0\varepsilon_0 H=0\,. \tag{2.8}$$

For the 2D waveguide structures, the vector equations can be decoupled to two different sets of equations: Transverse electric modes (TE) which do not contain the longitudinal electric field component, and transverse magnetic modes (TM) which do not contain the longitudinal magnetic field component. The vector wave equations for the transverse field of a two-dimensional structure are expressed in terms of the transverse electric fields

$$\frac{\partial^2 E_y}{\partial x^2}+\left(k_0^2 n^2-\beta^2\right)E_y=0 \tag{2.9}$$

for the TE polarization and the transverse magnetic fields

$$n^2\left[\frac{\partial}{\partial x}\left(\frac{1}{n^2}\frac{\partial H_y}{\partial x}\right)\right]+\left(k_0^2 n^2-\beta^2\right)H_y=0 \tag{2.10}$$

for the TM polarization. The propagation and transverse directions are supposed to be $z$ and $x$; $\beta$ is the propagation constant. The other field components of TE mode are expressed as

$$H_x=-\frac{\beta}{\omega\mu_0}E_y, \tag{2.11}$$

and

$$H_z=j\frac{1}{\omega\mu_0}\frac{\partial E_y}{\partial x}\,. \tag{2.12}$$

For the TM mode, the other field components are written as

$$E_x = \frac{\beta}{\omega \varepsilon_r \varepsilon_0} H_y, \tag{2.13}$$

and

$$E_z = j \frac{1}{n^2 \varepsilon_0 \omega} \frac{\partial H_y}{\partial x}. \tag{2.14}$$

### 2.1.2 Normalization, orthogonality and field confinement factor

Once all guided and complex modes of waveguide have been obtained, the transverse fields of waveguide can be expressed approximately as the linear superposition of eigenmodes:

$$\vec{E}_t(x,y,z) = \sum_{n=1}^{N} (a_n^+ e^{-j\beta_n z} + a_n^- e^{j\beta_n z}) \vec{e}_{tn}(x,y), \tag{2.15}$$

$$\vec{H}_t(x,y,z) = \sum_{n=1}^{N} (a_n^+ e^{-j\beta_n z} - a_n^- e^{j\beta_n z}) \vec{h}_{tn}(x,y), \tag{2.16}$$

For general (reciprocal) media, both guided and complex modes obey the same orthogonality in the same waveguide,

$$\iint (e_{tm} \times h_{tn} \mp e_{tn} \times h_{tm}) \cdot \hat{z} dA = 0 \quad for\ \beta_m \neq \pm \beta_n. \tag{2.17}$$

Especially for lossless media, the orthogonality can be expressed as,

$$\iint \left( e_{tm} \times h_{tn}^{*} + e_{tn}^{*} \times h_{tm} \right) \cdot \hat{z} dA = 0 \quad for\ \beta_m \neq \pm \beta_n. \tag{2.18}$$

We may normalize the field by setting the total guided power to unity, for general medium,

$$\frac{1}{4}\iint\left(e_{tn}\times h_{tn}^{*}+e_{tn}^{*}\times h_{tn}\right)\cdot\hat{z}dA=1. \tag{2.19}$$

For lossless media, it can be simplified as,

$$\frac{1}{4}\iint\left(e_{tn}\times h_{tn}\right)\cdot\hat{z}dA=1. \tag{2.20}$$

It is noted that for general media,

$$\frac{1}{4}\iint\left(e_{tn}\times h_{tn}\right)\cdot\hat{z}dA=N_n, \tag{2.21}$$

$N_n$ may not be equal to unity and may even be complex.

The confinement factor which described the ratio of the guided power in the guided area over the entire guided power, namely,

$$\Gamma=\frac{\iint\limits_{\text{Core}}\Re\left(E\times H^{*}\right)\cdot\hat{z}ds}{\iint\limits_{\text{Whole}}\Re\left(E\times H^{*}\right)\cdot\hat{z}ds}. \tag{2.22}$$

For the TE and TM modes in the 2D straight waveguides, we have

$$\Gamma_{\text{TE}}=\frac{\iint\limits_{\text{Core}}\left|E_y\right|^2\cdot dx}{\iint\limits_{\text{Whole}}\left|E_y\right|^2\cdot dx} \tag{2.23}$$

$$\Gamma_{\text{TM}}=\frac{\iint\limits_{\text{Core}}\Re\left(\frac{1}{n^2}\right)\left|H_y\right|^2\cdot dx}{\iint\limits_{\text{Whole}}\Re\left(\frac{1}{n^2}\right)\left|H_y\right|^2\cdot dx} \tag{2.24}$$

## 2.2 Finite Difference Scheme

One of the key issues in the field of guided-wave optics is the mode calculation. Vectorial mode analysis is greatly preferred due to its capability of handling polarization

dependence and coupling. Over the past several decades, a large number of analysis methods have been developed such as the imaginary distance beam propagation method [23], the finite-element method [24] , the method of lines [25, 26] and the finite difference method [22, 27-29]. Among these CAD tools, the finite difference method is one of the most well known numerical methods due to its simplicity and straightforward methodology[30].

### 2.2.1 First order finite difference scheme

The FDM based on graded index approximation was brought out firstly by Stern[27, 28], in which the discontinuity of the dielectric medium was matched by averaging the permittivity over meshes. Considering the sampled field $\phi_i$ and the nearby field $\phi_{i+1}$ illustrated in Fig. 1.

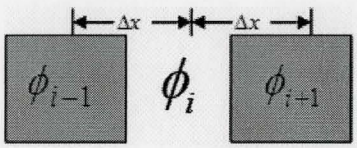


Fig. 1. Schematic of interfaces between sampled points

Using the Taylor series expansion, the second derivative of $\phi_i$ is expressed as

$$\frac{d^2\phi_i}{dx^2} = \frac{\phi_{i+1} + \phi_{i-1} - 2\phi_i}{\Delta x^2} + \mathrm{O}\left(x^3\right). \tag{2.25}$$

The TE modal equation (2.9) under this FDM scheme is discretized as

$$\frac{1}{\Delta x^2}\left(\hat{E}_y^{i+1} + \hat{E}_y^{i-1} - 2\hat{E}_y^i\right) + n_i^2 k_0^2 \hat{E}_y^i = \beta^2 \hat{E}_y^i, \tag{2.26}$$

and the TM modal equation under this FDM scheme is discretized as

$$\frac{1}{\Delta x^2}\left(\frac{1}{\left(n^2_{i+0.5}\right)}\bullet\hat{E}_x^{i+1}+\frac{1}{\left(n^2_{i-0.5}\right)}\bullet\hat{E}_x^{i-1}-\left(\frac{1}{\left(n^2_{i+0.5}\right)}+\frac{1}{\left(n^2_{i-0.5}\right)}\right)\hat{E}_x^{i}\right)+n_i^2k_0^2\hat{E}_x^i=\beta^2\hat{E}_x^i \quad , \tag{2.27}$$

where

$$\begin{aligned} n^2_{i+0.5}&=\frac{1}{2}\left(n_i^2+n_{i+1}^2\right)\\ n^2_{i-0.5}&=\frac{1}{2}\left(n_i^2+n_{i-1}^2\right)\end{aligned} \quad . \tag{2.28}$$

Combining all sampled points together the discretized modal equations become the eigen value problems,

$$\mathrm{A}\Phi=\beta^2\Phi \, . \tag{2.29}$$

Where A is a sparse matrix. The eigenvalue problem can be solved efficiently with Arnoldi iteration method [31].

It's noted that the truncation error of this scheme is $O\left(h^0\right)$ where $h$ is the mesh size. Furthermore, the accuracy can not by increased by using fine mesh scheme. By using the Taylor series expansion and from the matching conditions between the discontinuous interfaces, Vassallo provided an improved FDM scheme which has $O\left(h^2\right)$ truncation error when the interface is in the middle between the sampled points [29]. Later on, this work is developed by Chiou et al with the combination of the Generalized Douglas (GD) scheme [22]. The truncation error in this scheme is $O\left(h^4\right)$ in the uniform discretization cases irrespective of the location of the interfaces. For the completeness of this thesis, we give a brief derivation of this scheme.

### 2.2.2 High order finite difference scheme

We consider the magnetic field $\phi_i$ at an arbitrary sampled point, the nearby fields are denoted as $\phi_{i+1}, \phi_{i-1}$, respectively as shown in Fig. 1. Using the Taylor series expansion and matching the boundary conditions, $\phi_{i\pm1}$ can be expressed in terms of $\phi_i$ and its derivatives as

$$\phi_{i-1} = e_0\phi_i + e_1\phi_i^{'} + e_2\phi_i^{''} + e_3\phi_i^{(3)} + e_4\phi_i^{(4)} + e_5\phi_i^{(5)} + O\left(h^6\right), \tag{2.30}$$

$$\phi_{i+1} = f_0\phi_i + f_1\phi_i^{'} + f_2\phi_i^{''} + f_3\phi_i^{(3)} + f_4\phi_i^{(4)} + f_5\phi_i^{(5)} + O\left(h^6\right). \tag{2.31}$$

The General Douglas operators are derived by omitting the high order terms,

$$\phi_i^{'} \approx \frac{f_2\phi_{i-1} + \left(f_0e_2 - e_0f_2\right)\phi_i - e_2\phi_{i+1}}{e_1f_2 - f_1e_2} \equiv D_x\phi_i, \tag{2.32}$$

$$\phi_i^{''} \approx \frac{f_1\phi_{i-1} + \left(f_0e_1 - e_0f_1\right)\phi_i - e_1\phi_{i+1}}{e_2f_1 - f_2e_1} \equiv D_x^2\phi_i. \tag{2.33}$$

By combining(2.30),(2.31), we have

$$\frac{f_1\phi_{i-1} + (f_0e_1 - e_0f_1)\phi_i - e_1\phi_{i+1}}{e_2f_1 - e_1f_2} = \phi_i^{''} - \frac{(f_3e_1 - e_3f_1)\phi_i^{(3} + (f_4e_1 - e_4f_1)\phi_i^{(4)} + (f_5e_1 - e_5f_1)\phi_i^{(5)}}{e_2f_1 - f_2e_1} + O\left(h^4\right). \tag{2.34}$$

The above expression is approximated with

$$\phi_i^{''} \approx \frac{D_x^2\phi_i}{1 + g_1D_x + g_2D_x^2}. \tag{2.35}$$

Substituting (2.35)into the Helmholtz equation leads to

$$\frac{D_x^2\phi_i}{1 + g_1D_x + g_2D_x^2} + k_0^2\phi_i = \beta^2\phi_i. \tag{2.36}$$

Eq. (2.36) can be denoted as

$$A'\Phi = \beta^2 C\Phi . \tag{2.37}$$

This eigenvalue problem can be solved efficiently with Arnoldi iteration method. The coefficients $e_i$ and $f_i$ are given in the Appendix A.

## 2.3 Numerical Boundary Conditions

### 2.3.1 Zero boundary conditions

A potential problem with the finite difference method is that it requires the structure to be enclosed in a metal box, in order to truncate the computation window. If the computation window is large enough, the electrical field for TE guided wave or the magnetic field for TM guided wave can be seen decayed to zero. However, the parasite reflections may happen for radiative wave since they will be reflect back at the boundary thereby affect the simulation results. Further, if the computation window is not large enough and the guided wave may not decay to zero, even the fundamental modes will be disturbed. Therefore, the advanced boundary conditions are desired to fulfill the potential of the numerical method.

### 2.3.2 Perfect matching layers (PML)

Assume the computation region enclosing the studied structures is terminated at the edges by the null boundary conditions. We can place the perfectly matched layer (PML) adjacent to the boundary to minimize the reflections from the boundary [32, 33].

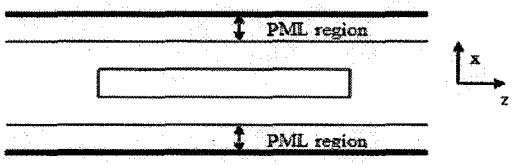


Fig. 2. Schematic of the computation window

By this computation model, the entire mode spectrum will be discretized into two categories: guided modes and complex modes [34]. Both possess the normal mode characteristics such as the orthogonality and normalization. The PML region is helpful to reduce the parasitic reflection, therefore the closed waveguide structure can be considered as an open one. In this work, we employ the complex coordinate stretching PML scheme [35]. In the real medium, the mesh is real and unaffected; in the PML region, the stretching factor is given by

$$s_x = \kappa_x - j\frac{\sigma_x}{\omega\varepsilon_0 n^2}. \tag{2.38}$$

The parameters $\sigma_x$ in the imaginary part controls the absorption of the propagating waves in the PML region, the real part $\kappa_x$ can help to attenuate the evanescent waves. Practically, the parameter $\sigma_x$ usually takes the following form

$$\sigma = \sigma_{\max}(\frac{\rho}{l_{PML}})^m, \qquad m = 1, 2, 3, \ldots \tag{2.39}$$

where $l_{PML}$ is the PML thickness and $\rho$ is the distance from the origin point of the PML. The relationship between $\sigma_{\max}$ and the reflection coefficient $R$ at the interface between the real and PML region is given by

$$R = \exp\left[-\frac{2\sigma_{\max}}{c\varepsilon_0 n}\int_0^{d_{PML}}(\frac{\rho}{l_{PML}})^m d\rho\right], \tag{2.40}$$

where $c$ is the light speed in free space. Combining the equations above, the stretching factor $s_x$ is

$$s(\rho) = 1 - j\frac{\sigma}{\omega\varepsilon_0 n^2} = 1 - j\frac{\lambda}{4\pi n l_{PML}}\left[(m+1)\ln\frac{1}{R}\right](\frac{\rho}{l_{PML}})^m. \tag{2.41}$$

## 2.4 Validation of the Mode Solvers

### 2.4.1 TE modes in Multi-mode slab waveguide

We take the multi mode dielectric slab waveguide structure (Fig. 3) as an example, the parameters used in simulation are as follows: $n_s$=3.2, $n_{core}$=3.5, $n_c$=1.0, the wavelength is 500nm, and the section lengths are all 0.5 um.

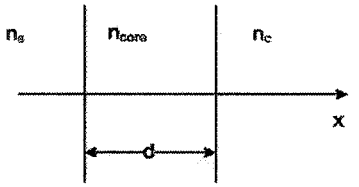


Fig. 3. Schematic of multi- mode slab structure.

Using the 4th order FDM with the zero boundary condition facilitated by PML, it is found that this structure can support 3 TE modes. For comparison, we also use smooth transition method to calculate the guide mode of this structure [36]. The results of effective index calculated by FD4 and smooth transition method are shown in

Table 1 and the field patterns are shown in Fig. 4. The results clearly show the accuracy of the high order FDM. The parameters used in calculation are: mesh size is

5nm, computation window is 1.5μm, reflection coefficient is 0.1 and the thickness of PML is 50nm.

Table 1. Effective index of guided modes (TE)

| Mode No. | $TE_0$ | $TE_1$ | $TE_2$ |
|---|---|---|---|
| FD4 | 3.47343258465 | 3.39376054353201 | 3.26398099338036 |
| Analytical | 3.47343259501 | 3.39376059456825 | 3.26399240834809 |

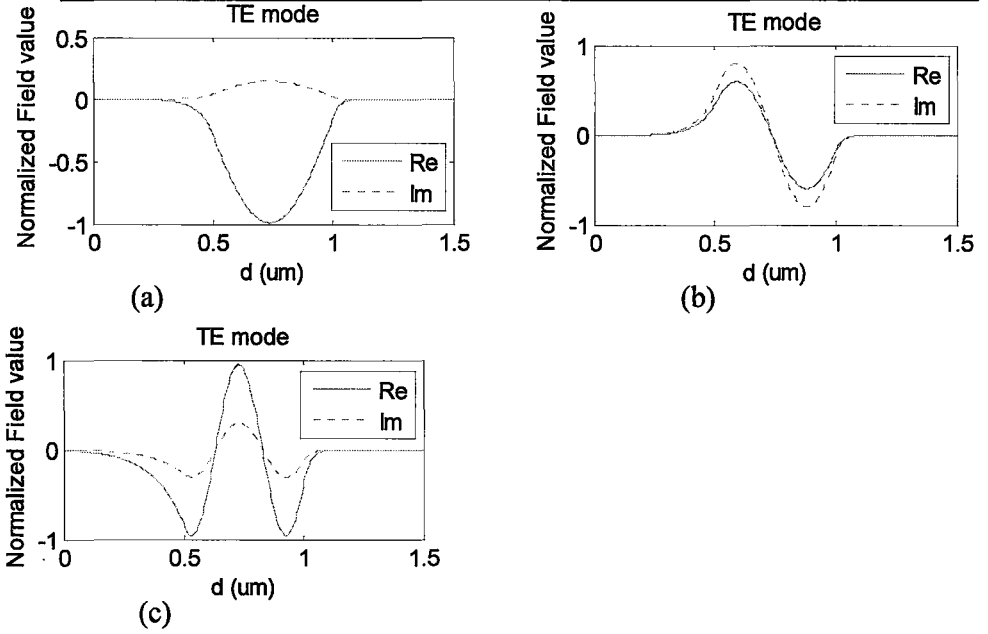


Fig. 4. Guided mode profiles of dielectric multi- modes slab waveguide.

Due to the presence of PML, the complex modes are split into two types, one is PML mode whose energy focused in PML region and another one is quasi-leaky mode which grows towards cladding and decaying in the PML region (Fig. 5).

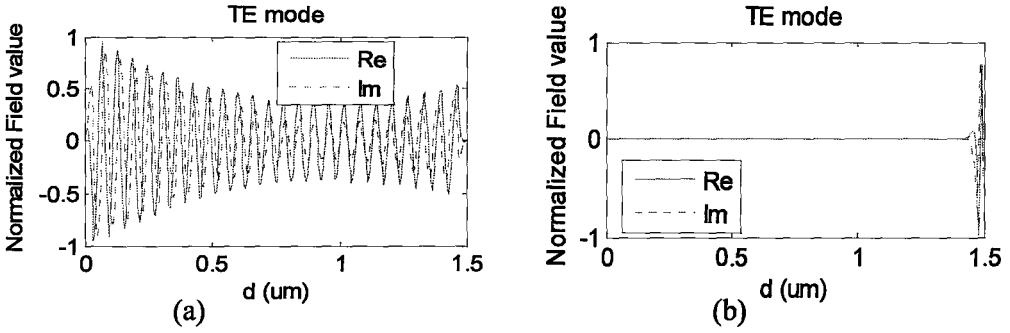


Fig. 5. Mode profiles of complex modes. (a) Quasi-leaky mode, (b) PML mode.

### 2.4.2 TE modes in Single-mode slab waveguide

The single-mode condition for symmetric slab waveguide of step-index is given by,

$$\frac{\lambda}{2d} > 2\sqrt{2}\bar{n}\sqrt{\Delta} \tag{2.42}$$

where $\Delta = \frac{n_1 - n_2}{\bar{n}}$ is the relative refractive index difference, $\bar{n} = \frac{n_1 + n_2}{2}$ is the average between the core and the cladding and 2d is the full width of the waveguide. We can design the single mode symmetric slab waveguide according to this criterion. The designed structure is the shown in Fig. 3, the core width is 100nm, $n_s$=1.0, $n_{cl}$=1.0, $n_c$=3.5. The electric field patterns of $TE_0$ and one of the quasi-leaky mode s are shown in Fig. 6; the effective indexes are listed in Table 2.

Table 2. Effective index of the single mode slab waveguide (TE)

| Mode | TE0 | Quasi-leaky mode |
|---|---|---|
| Effective Index | 2.52269110177425 | 0.04691885836580 - 1.18713297025981i |

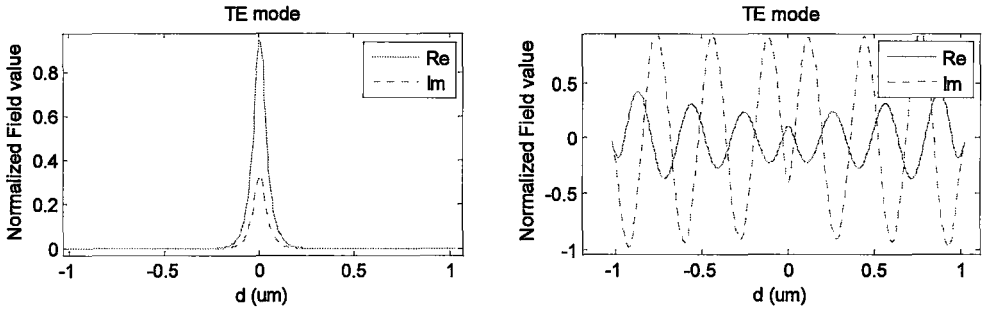


Fig. 6. Electric field distributions of $TE_0$ mode and a quasi-leaky mode

### 2.4.3 TM modes in Multi-mode slab waveguide

The multi mode dielectric slab waveguide structure (TM) is shown in Fig. 3, the parameters used in simulation are as follows: $n_s$=3.2, $n_{core}$=3.5, $n_c$=1.0, wavelength is 500nm, the section length are all 0.5 um. The effective indexes calculated by FD4 and by analytical method are shown in Table 3, the field distributions of guided modes are shown in Fig. 7.

Table 3. Effective index of the multi- modes slab waveguide(TM)

| Mode No. | $TM_0$ | $TM_1$ | $TM_2$ |
|---|---|---|---|
| FD4 | 3.47038303976 | 3.38216642802250 | 3.24323871540516 |
| Analytical | 3.47038304155 | 3.38216646140793 | 3.24328640147197 |

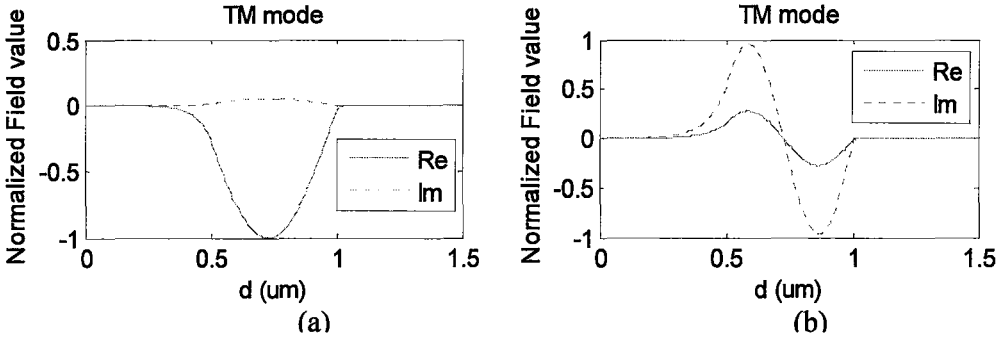

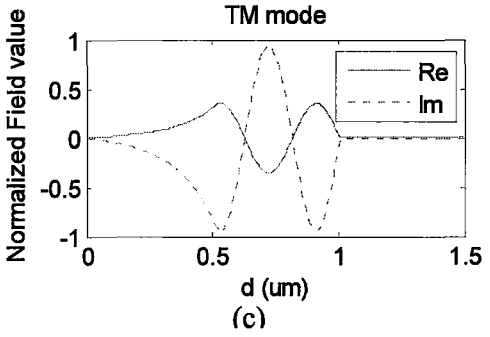


Fig. 7. Mode profiles of TM guided modes (a) $TM_0$, (b) $TM_1$, (c) $TM_2$.

### 2.4.4 TM modes in Single-mode slab waveguide

The designed structure is the same with Fig. 3, the core width is 50nm, $n_s$=1.0, $n_c$=1.0, $n_{core}$=3.5.

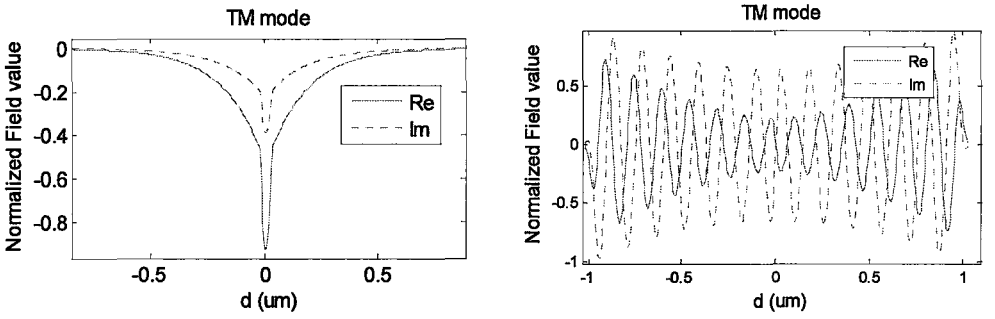


Fig. 8. Field distribution of TM0 mode (a) and a quasi-leaky TM mode (b).

The magnetic field patterns of $TM_0$ and a quasi-leaky mode are shown in Fig. 8. The effective indexes are list in Table 4.

Table 4. Effective index of the single mode slab waveguide (TM)

| Mode | $TM_0$ | Quasi-leaky mode |
|---|---|---|
| Effective Index | 1.10311363663869 | 0.08272982067527 - 3.124139645110l8i |

# Chapter 3

# Complex Mode Matching Method for Periodic Waveguide Structures

## 3.1 Introduction

There have been extensive literatures on the subject of theoretical modeling and analysis of optical waveguide Bragg gratings in which the coupled-mode theory (CMT) and/or the coupled-wave approach (CWA) are most popular [9, 37, 38]. The CMT and/or CWA are physically intuitive, mathematically simple, and highly accurate especially for shallow gratings with relatively weak index corrugations. For Bragg gratings with strong index corrugations, more rigorous approach such as the mode-matching methods (MMM)[21], the bi-directional beam propagation method (Bi-BPM) [39, 40], and the finite-difference time-domain (FDTD) method [19], can all be used with different levels of complexities and accuracy. Among all the methods mentioned above, MMM is considered as an efficient and rigorous method in dealing with periodical structures among all the approaches. In MMM approach, the waveguide grating is considered as two periodical alternative sections, section A and section B. In each section the total propagating field is expressed as the eigenmodes superposition. Using the continuity conditions of tangential components of electric and magnetic field at the boundaries, as well as orthogonality relations, the different sections then can be linked by a scattering matrix. The total reflection and transmission is calculated by cascading the scattering matrix instead of transfer matrix method to enhance the numerical stability [41]. Also, we can apply the

Floquet theorem in the mode-matching method on the assumption of perfect periodicity so that the eigenmodes or Floquet-Bloch waves of the grating structures can be obtained [42, 43].

## 3.2 Transfer Matrix Formulations

For a single waveguide discontinuity (Fig. 9), the governing mode equation for different waveguide sections is a 1D Helmholtz equation,

$$\left(\frac{\partial^2}{\partial x^2}+k^2n^2-\beta^2\right)\psi(x)=0. \tag{3.1}$$

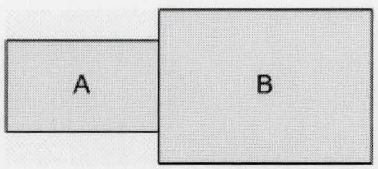


Fig. 9. A single discontinuity

The mode spectrum including guided and complex modes used in the modal expansion are calculated by fourth order finite difference method together with complex coordinate stretching formulation of PMLs.

Assume totally N modes in waveguide A and M modes in waveguide B, once all guided and complex modes of waveguide have been obtained, the transverse fields of waveguide A and waveguide B can be expressed approximately as the linear superposition of eigenmodes:

$$\vec{E}_t^A(x,y,z)=\sum_{n=1}^{N}(a_n^+e^{-j\beta_n^Az}+a_n^-e^{j\beta_n^Az})\vec{e}_{tn}^A(x,y), \tag{3.2}$$

$$\vec{H}_t^A(x,y,z)=\sum_{n=1}^{N}(a_n^+e^{-j\beta_n^Az}-a_n^-e^{j\beta_n^Az})\vec{h}_{tn}^A(x,y), \tag{3.3}$$

$$\vec{E}_t^B(x,y,z)=\sum_{m=1}^{M}(b_m^+e^{-j\beta_m^B z}+b_m^-e^{j\beta_m^B z})\vec{e}_{tm}^B(x,y), \tag{3.4}$$

$$\vec{H}_t^B(x,y,z)=\sum_{m=1}^{M}(b_m^+e^{-j\beta_m^B z}-b_m^-e^{j\beta_m^B z})\vec{h}_{tm}^B(x,y). \tag{3.5}$$

Where $t$ denotes the transverse components, $\beta_{n(m)}^{A(B)}$ is the propagation constant of the $n$th ($n$th) mode in waveguide A (B); $\vec{e}_{tn(m)}^{A(B)}, \vec{h}_{tn(m)}^{A(B)}$ are the $n$th ($m$th) transverse electric field and magnetic fields vectors of the A (B) waveguide, respectively; and $a_n^+, a_n^-, b_m^+, b_m^-$ are the amplitudes of forward and backward waves of the $n_{th}$ nth mode in waveguide A and $m_{th}$ mode in waveguide B, respectively.

Applying the continuity conditions of tangential components of electrical magnetic field at the interfaces between neighbouring sections, we have,

$$\sum_{n=1}^{N}(a_n^+ + a_n^-)\vec{e}_{tn}^A(x,y)=\sum_{m=1}^{M}(b_m^+ + b_m^-)\vec{e}_{tm}^B(x,y), \tag{3.6}$$

$$\sum_{n=1}^{N}(a_n^+ - a_n^-)\vec{h}_{tn}^A(x,y)=\sum_{m=1}^{M}(b_m^+ - b_m^-)\vec{h}_{tm}^B(x,y). \tag{3.7}$$

Cross product (3.6) with $\vec{h}_{tk}^B$, cross product (3.7) with $\vec{e}_{tk}^B$, respectively, then integrate over the waveguide cross-section, we can obtain

$$\sum_{n=1}^{N}(a_n^+ + a_n^-)<\vec{e}_{tn}^A, \vec{h}_{tk}^B>=\sum_{m=1}^{M}(b_m^+ + b_m^-)<\vec{e}_{tm}^B, \vec{h}_{tk}^B>, \tag{3.8}$$

$$\sum_{n=1}^{N}(a_n^+ - a_n^-)<\vec{e}_{tk}^B, \vec{h}_{tn}^A>=\sum_{m=1}^{M}(b_m^+ - b_m^-)<\vec{e}_{tk}^B, \vec{h}_{tm}^B). \tag{3.9}$$

The inner product of the field vectors is defined as,

$$< \vec{e}, \vec{h} >= \frac{1}{2} \iint_S (\vec{e} \times \vec{h}) \cdot \hat{z}\, ds . \tag{3.10}$$

With the help of orthogonality relations between the modes, i.e.

$$\frac{1}{2} \iint_S (\vec{e}_{tm} \times \vec{h}_{tn}) \cdot \hat{z}\, ds = < \vec{e}_{tm}, \vec{h}_{tn} > \delta_{mn}, \tag{3.11}$$

we get the amplitudes of waveguide B in terms of amplitudes waveguide A ,

$$b_m^+ = \sum_{n=1}^{N} a_n^+ \left[ \frac{< \vec{e}_{tn}^A, \vec{h}_{tm}^B > + < \vec{e}_{tm}^B, \vec{h}_{tn}^A >}{2 < \vec{e}_{tm}^B, \vec{h}_{tm}^B >} \right] + \sum_{n=1}^{N} a_n^- \left[ \frac{< \vec{e}_{tn}^A, \vec{h}_{tm}^B > - < \vec{e}_{tm}^B, \vec{h}_{tn}^A >}{2 < \vec{e}_{tm}^B, \vec{h}_{tm}^B >} \right], \tag{3.12}$$

$$b_m^- = \sum_{n=1}^{N} a_n^+ \left[ \frac{< \vec{e}_{tn}^A, \vec{h}_{tm}^B > - < \vec{e}_{tm}^B, \vec{h}_{tn}^A >}{2 < \vec{e}_{tm}^B, \vec{h}_{tm}^B >} \right] + \sum_{n=1}^{N} a_n^- \left[ \frac{< \vec{e}_{tn}^A, \vec{h}_{tm}^B > + < \vec{e}_{tm}^B, \vec{h}_{tn}^A >}{2 < \vec{e}_{tm}^B, \vec{h}_{tm}^B >} \right]. \tag{3.13}$$

The overlapping integral in 1D case may be further simplified. Taking TE mode as an example, we have

$$< e_x, h_y >= \frac{1}{2} \int -e_x h_y dx = \int \frac{\beta}{2\omega\mu_0} e_y^2 dx , \tag{3.14}$$

$$< e_y^A, h_x^B >= \frac{1}{2} \int e_y^A \frac{\beta^B}{\omega\mu_0} e_y^B dx = \frac{\beta^B}{2\omega\mu_0} \int e_y^A e_y^B dx , \tag{3.15}$$

$$< e_y^B, h_x^A >= \frac{1}{2} \int e_y^B \frac{\beta^A}{\omega\mu_0} e_y^A dx = \frac{\beta^A}{2\omega\mu_0} \int e_y^A e_y^B dx , \tag{3.16}$$

We can put them in the matrix form,

$$\begin{bmatrix} B^+ \\ B^- \end{bmatrix} = \begin{pmatrix} T_{11} & T_{12} \\ T_{21} & T_{22} \end{pmatrix} \begin{bmatrix} A^+ \\ A^- \end{bmatrix}. \tag{3.17}$$

## 3.3 Scattering Matrix Formulations

As the Bragg grating contains a large number of periods, it's well known that the scattering matrix performing more stable comparing to the transfer matrix. Now we consider multiple waveguide discontinuities shown in Fig. 10.

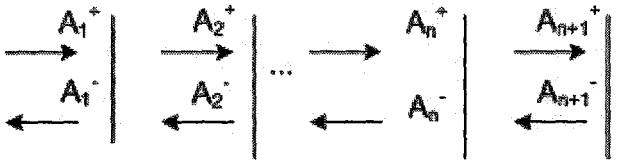


Fig. 10: Multiple waveguide discontinuities.

The values of the forward and backward waves at the left sides of the $1_{st}$, $2_{rd}$, ..., $n_{th}$, and $(n+1)_{th}$ discontinuities are represented by $A_1^+$, $A_1^-$, $A_2^+$, $A_2^-$ ... $A_n^+$, $A_n^-$, $A_{n+1}^+$, $A_{n+1}^-$, respectively. The S matrix formulation is

$$\begin{bmatrix} A_{n+1}^+ \\ A_1^- \end{bmatrix} = \begin{bmatrix} T_{1,n+1} & R_{n+1,1} \\ R_{1,n+1} & T_{n+1,1} \end{bmatrix} \begin{bmatrix} A_1^+ \\ A_{n+1}^- \end{bmatrix}, \tag{3.18}$$

where

$$\begin{aligned} T_{1,n+1} &= T_{n,n+1}(I - R_{n,1}R_{n,n+1})^{-1}T_{1,n} \\ R_{n+1,1} &= T_{n,n+1}(I - R_{n,1}R_{n,n+1})^{-1}R_{n,1}T_{n+1,n} + R_{n+1,n} \\ R_{1,n+1} &= T_{n,1}(I - R_{n,n+1}R_{n,1})^{-1}R_{n,n+1}T_{1,n} + R_{1,n} \\ T_{n+1,1} &= T_{n,1}(I - R_{n,n+1}R_{n,1})^{-1}T_{n+1,n} \end{aligned} \tag{3.19}$$

## 3.4 Periodic Doubling Algorithms

If the structure contains symmetric cells, then we can choose the cascading and doubling method to save the computation effort. The main idea is to find the equivalent larger

scattering cells instead of layer by layer cascading. Given three arbitrary discontinuities denoted by $n, m, k$, respectively. The scattering matrix between them is given by,

$$\begin{bmatrix} A_m^+ \\ A_n^- \end{bmatrix} = \begin{bmatrix} T_{nm} & R_{mn} \\ R_{nm} & T_{mn} \end{bmatrix} \begin{bmatrix} A_n^+ \\ A_m^- \end{bmatrix}, \tag{3.20}$$

$$\begin{bmatrix} A_k^+ \\ A_m^- \end{bmatrix} = \begin{bmatrix} T_{mk} & R_{km} \\ R_{mk} & T_{km} \end{bmatrix} \begin{bmatrix} A_m^+ \\ A_k^- \end{bmatrix}. \tag{3.21}$$

Thus the scattering matrix between $k$ and $n$ can be obtained,

$$\begin{bmatrix} A_k^+ \\ A_n^- \end{bmatrix} = \begin{bmatrix} T_{nk} & R_{kn} \\ R_{nk} & T_{kn} \end{bmatrix} \begin{bmatrix} A_n^+ \\ A_k^- \end{bmatrix}, \tag{3.22}$$

where

$$\begin{aligned} T_{n,k} &= T_{mk}(I - R_{mn}R_{mk})^{-1}T_{nm} \\ R_{k,n} &= T_{mk}(I - R_{mn}R_{mk})^{-1}R_{mn}T_{km} + R_{km} \\ R_{n,k} &= T_{mn}(I - R_{mk}R_{mn})^{-1}R_{mk}T_{nm} + R_{nm} \\ T_{k,n} &= T_{mn}(I - R_{mk}R_{mn})^{-1}T_{km} \end{aligned} \tag{3.23}$$

Taking the advantage of symmetric, we can firstly calculate one cell, then using the results to calculate a double period and so on. For arbitrary N periods, N can be decomposed to $N = 2^{n_1} + 2^{n_2} + \cdots + 2^{n_m}$ or $N = 2^{n_1} + 2^{n_2} + \cdots + 2^{n_m} + 1$ depends on whether N is even or odd. Only $\max(n_1, \cdots, n_m)$ iterations needed since other value is obtained during calculating $\max(n_1, \cdots, n_m)$.

## 3.5 Floquet Theorem

For periodical structures, Floquet-Bloch approach takes the advantage over the others in band analysis, as the Floquet mode play the same role in a periodical structure as the

guided modes in a waveguide, so that it can disclose more insightful physical phenomena. Our analysis model is using Bloch-Floquet mode approach within the framework of MMM[42, 43], where FB modes is defined as the eigenmodes of the transfer matrix. Through this way, the Floquet mode is a combination of the forward waves and backward waves.

From the formulations derived in Chapter 4.2, the scattering matrix for a single period of periodical structure is given as

$$\begin{bmatrix} A_{k+1}^{+} \\ A_{k}^{-} \end{bmatrix} = \begin{pmatrix} S_{11} & S_{12} \\ S_{21} & S_{22} \end{pmatrix} \begin{bmatrix} A_{k}^{+} \\ A_{k+1}^{-} \end{bmatrix}. \tag{3.24}$$

One can derive the transfer matrix from the scattering matrix,

$$\begin{pmatrix} A_{k+1}^{+} \\ A_{k+1}^{-} \end{pmatrix} = \begin{pmatrix} T_{11} & T_{12} \\ T_{21} & T_{22} \end{pmatrix} \begin{pmatrix} A_{k}^{+} \\ A_{k}^{-} \end{pmatrix} \tag{3.25}$$

The relations linking the scattering matrix and transfer matrix are

$$\begin{aligned} T_{11} &= S_{11} - S_{12} S_{22}^{-1} S_{21} \\ T_{12} &= S_{12} S_{22}^{-1} \\ T_{21} &= -S_{22}^{-1} S_{21} \\ T_{22} &= S_{22}^{-1} \end{aligned} \tag{3.26}$$

Using scattering matrix to obtain the transfer matrix can avoid the numerical instability when cascading the propagation matrix.

By applying the Floquet theorem, the transfer matrices of one grating period is related to each other by

$$\begin{pmatrix} A_{k+1}^{+} \\ A_{k+1}^{-} \end{pmatrix} = \exp(-jK\Lambda) \begin{pmatrix} A_{k}^{+} \\ A_{k}^{-} \end{pmatrix}. \tag{3.27}$$

Combining eq.(3.25) with eq. (3.27) will lead to the eigen-equations for the Floquet-Bloch modes as follows:

$$\begin{pmatrix} T_{11} & T_{12} \\ T_{21} & T_{22} \end{pmatrix} \begin{pmatrix} A^{+} \\ A^{-} \end{pmatrix} = \exp(-jK\Lambda) \begin{pmatrix} A^{+} \\ A^{-} \end{pmatrix}. \tag{3.28}$$

Note that we deliberately drop the sub-script $k$ for the $k$-th period as the same equation applies to any of the grating sections. Eqs. (3.28) can be solved by a standard matrix eigen-value solver and the eigenvalues $\mathrm{K}_l$ and its corresponding eigen vector $\mathbf{A}_l = \begin{pmatrix} A^{+} \\ A^{-} \end{pmatrix}$ can be readily obtained.

The transverse electric fields of the transverse electric field for the TE modes for each $\mathrm{K}_l$ ($l = 1...N$) are expressible as

$$\mathbf{E}_l(x,z) = \sum_{k=1} \left\{ a_{lk}^{+} e^{-j\beta_k z} + a_{lk}^{-} e^{+j\beta_k z} \right\} \mathbf{e}_k(x) \tag{3.29}$$

$$\mathbf{H}_l(x,z) = \sum_{k=1} \left\{ a_{lk}^{+} e^{-j\beta_k z} - a_{lk}^{-} e^{+j\beta_k z} \right\} \mathbf{h}_k(x) \tag{3.30}$$

where $a_{lk}^{+}, a_{lk}^{-}$ are the k-th components of $l$-th column eigenvector $\mathbf{A}(l)$ and $\mathbf{e}_k(x)$, $\mathbf{h}_k(x)$ are the $k$-th local mode. The equivalent effective index of the Floquet mode is defined by

$$N_{eq} = \mathrm{K}/k_0. \tag{3.31}$$

# Chapter 4

# Analysis of Deep Bragg Gratings with High Index Contrast Corrugations

## 4.1 Introduction

One of the key concepts in design and analysis of grating structures is the Bragg condition at which the constructive interference between the forward and the backward propagating waves occurs. For the 1st-order gratings consisting of two sub-sections of lengths $\Lambda_a$ and $\Lambda_b$ , respectively, for the unit cells (as shown in Figure 1), the Bragg conditions are expressed as

$$\frac{2\pi}{\lambda_B} N_m \Lambda_m = \frac{\pi}{2} \tag{4.1}$$

or

$$\Lambda_m = \frac{\lambda_B}{4N_m}, \tag{4.2}$$

where $N_m$ ( $m = a, b$ ) are the effective indices of the fundamental local modes in the grating sections. It is a widely held belief that the Bragg wavelength corresponds to the peak of the reflection spectrum based on the fact that all the reflected waves are added in-phase due to constructive interference of the reflected waves from each of the grating interfaces. The conventional Bragg condition is, however, valid only for the gratings of weak index corrugations in which the dominant Floquet wave components of the fundamental guided modes are considered in the analysis. As the grating becomes

stronger, the high-order space harmonic waves and/or the radiative waveguide modes start to play increasingly more important roles. Physically, the interaction between the electromagnetic waves and the periodic grating structures gives rise to coupling between the space harmonics of the guided and radiation modes. Consequently, portion of energy is stored in the vicinity of the grating interfaces. The reactive stored energy is responsible for the blue shift of the peak wavelength from the conventional Bragg wavelength. It is pointed out by J. Ctyroky that the shift towards the wavelength shorter than the conventional Bragg wavelength is expected as higher-order waveguide modes with smaller effective indices are involved [42, 43]. To illustrate this effect, a general Bragg grating as shown in Fig. 11 is taken as an example. The parameters used are $n_s$=1.52, $n_c$=1.0 and $n_g$=1.53, the designed central wavelength is 650nm in accordance to the conventional Bragg condition (eq.(4.1)). The lengths of the grating sections are: $\Lambda_a$= 0.106456 μm and $\Lambda_b$=0.106553 μm, respectively. The thickness of the guiding layer is 2.4um. The etching depth equals to 0.5 um, and the number of periods is 1793.

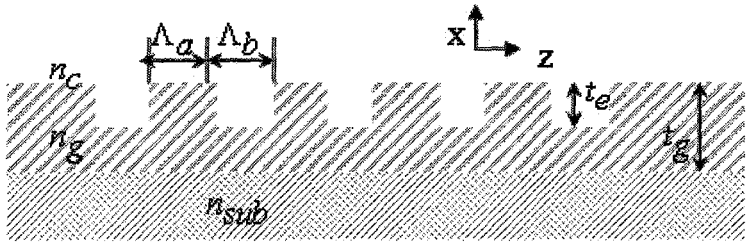


Fig. 11. A typical Bragg grating structure consisting of two-element unit cells.

The reflection spectrum of the fundamental TE mode is analyzed by the complex mode matching method (MMM) and BiBPM and illustrated in Fig. 13. It is noted that we have assumed a computational model in which the computation region enclosing the

grating structures is terminated at the edges by the null boundary conditions. Further, we place the perfectly matched layer (PML) adjacent to the boundary to minimize the reflections from the boundary (Fig. 12.).

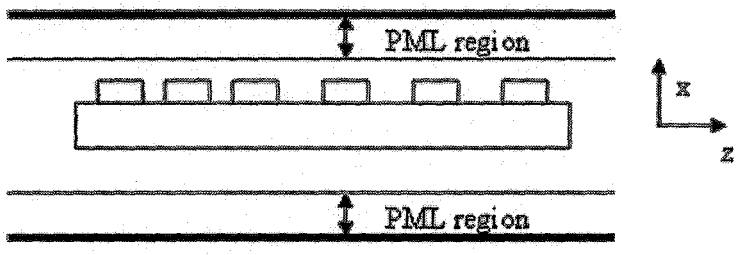


Fig. 12. Schematic of the computation window.

Parameters used in MMM are summarized as follows: the computational window size is 8.4 μm including a perfectly matched layer (PML) of 1 μm thickness on each side, the reflection coefficient is 0.001. Although the waveguide is single mode, we have employed total of 40 modes including the quasi-leaky and PML modes in the mode expansion. For the sake of comparison, we also show the reflection spectrum calculated by using only the guided modes, which exhibits its peak wavelength in accordance with the conventional Bragg wavelength. For the rigorous analysis, the central wavelength of the peak reflectivity is shifted to 649.8nm from the designed wavelength of 650nm.

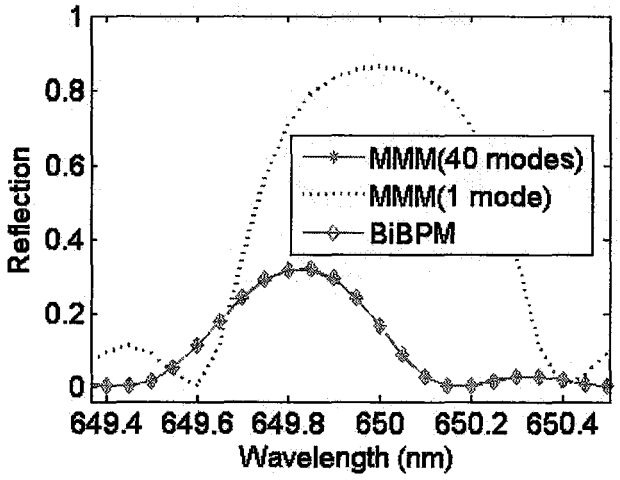


Fig. 13. Reflection spectrum of the fundamental TE mode of the deeply etched grating structure in Fig. 11. The parameters are $n_s$=1.52, $n_g$=1.53, $n_c$=1, $\Lambda_a$= 0.106456 μm and $\Lambda_b$=0.106553 μm, and etching depth $t_e$=0.5μm. The central wavelength 650.0nm designed according to the conventional Bragg condition corresponds to the prediction based on only the fundamental modes (dashed line), whereas the actual central wavelength is shifted to 649.8nm as calculated by the rigorous mode-matching method (solid line with star) and high order BiBPM (solid line with diamond).

It is however not clear how we may design the grating structures, e.g., the grating period, to obtain the desired peak wavelength when the index corrugations of the gratings are strong. This question will be discussed and answered in this Chapter.

## 4.2 Floquet Mode in Bragg Gratings

We are using Floquet-Bloch approach described in previous chapter as analysis model. To investigate the band structure of the Bragg grating, we choose the structure shown in Fig. 11 as an example. Two different etching depths 0.5um and 1.0um are considered; the other parameters are the same as those used in Fig. 13.

Fig. 14 and Fig. 15 display the band dispersion relations for TE polarization, i.e., the real and imaginary parts of the normalized propagation constant of the fundamental Floquet-Bloch mode as functions of wavelength. It is demonstrated that the center of the stop-band corresponds to the peak wavelength of the reflection spectrum as expected and shifts to shorter wavelength from the conventional Bragg wavelength.

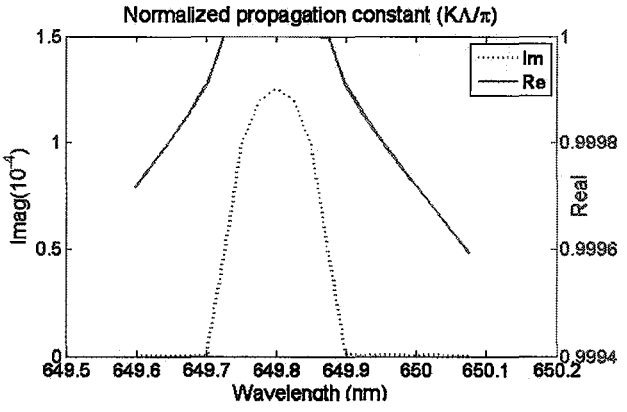


Fig. 14.Normalized propagation constant of the fundamental Floquet-Bloch mode with respect to wavelength, etching depth=0.5μm, other parameters are the same as Fig. 13. Solid: real part; dotted: imaginary part.

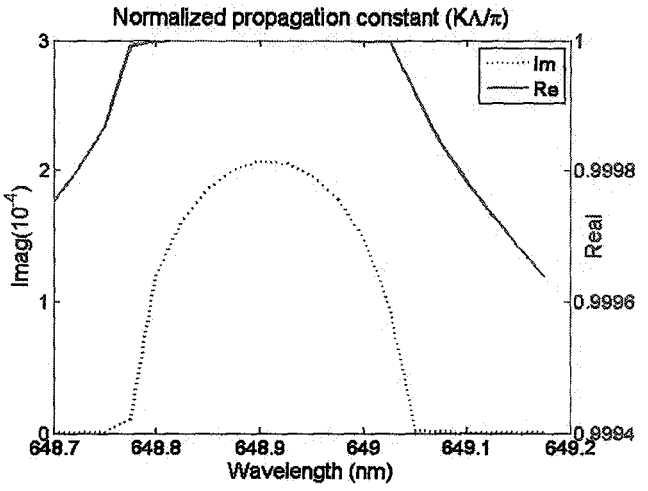


Fig. 15.Normalized propagation constant of the fundamental Floquet-Bloch mode with respect to wavelength, etching depth=1μm, other parameters are the same as Fig. 13. Solid: real part; dotted: imaginary part.

## 4.3 Iterative Method

The above analysis has clearly demonstrated that the peak of wavelength of the strongly corrugated gratings is consistent with the center of the stop-band for the fundamental Floquet-Bloch mode and shifted from the conventional Bragg wavelength based on the fundamental local modes of the waveguide. Yet, it is still not clear how to design the grating period for a given index corrugation so that we can realize the reflection peak or the center of the stop-band at a given wavelength. In this section, we will show that we can apply a simple iterative method starting from the conventional Bragg condition as follows.

The central wavelength can be approximated by the equivalent effective index of the fundamental Floquet mode with the relation,

$$\lambda = 2\Lambda \cdot \mathrm{Re}\left(N_{eq}\right), \tag{4.3}$$

where $\lambda$ is the central wavelength, and $N_{eq}$ is the equivalent effective index of the fundamental Floquet mode corresponding to the central wavelength, and $\Lambda$ is the period length. Taking the derivative of $\Lambda$ for both sides,

$$\frac{\partial \lambda}{\partial \Lambda} = 2\left( N_{eq} + \frac{\partial \mathrm{Re}\left(N_{eq}\right)}{\partial \Lambda} \cdot \Lambda \right). \tag{4.4}$$

Since $N_{eq} > \frac{\partial \mathrm{Re}\left(N_{eq}\right)}{\partial \Lambda} \cdot \Lambda$, $\frac{\partial \lambda}{\partial \Lambda}$ is always a positive function. Now assume that the central wavelength we designed for is $\lambda_0$. We first design the grating parameters, namely, $\Lambda_1$ (For the sake of simplicity, take the example of $\Lambda_a$ shown in Fig. 11, the same approach can be used to calculate $\Lambda_b$), according the conventional Bragg conditions eq. (4.1). Consequently, we obtain a different central wavelength $\lambda_A$ corresponding to the originally designed grating period is $\Lambda_1$. Now we can introduce the period shift $\delta\Lambda$ defined as,

$$\delta\Lambda = \frac{\lambda_0 - \lambda_A}{\lambda_A}\Lambda_1. \tag{4.5}$$

Therefore the newly corrected period is $\Lambda_2 = \Lambda_1 + \delta\Lambda$. Due to the period change, the central wavelength will experience a shift depending on the sign of $\delta\Lambda$. Using Taylor expansion and omitting the high order items,

$$\lambda_B \approx \lambda_A + \frac{\partial \lambda}{\partial \Lambda} \cdot \delta\Lambda \tag{4.6}$$

where $\lambda_B$ is the shifted central wavelength with the corrected period $\Lambda_2$ .After some straightforward derivations, we obtain

$$\delta\lambda_2 = \delta\lambda_1 \left(1 - \frac{\partial \lambda}{\partial \Lambda} \cdot \frac{\Lambda_1}{\lambda_A}\right) \tag{4.7}$$

where $\delta\lambda_2 = \lambda_0 - \lambda_B$ and $\delta\lambda_1 = \lambda_0 - \lambda_A$.

Taking absolute value on both sides,

$$|\delta\lambda_2| = |\delta\lambda_1| \cdot \left|\left(1 - \frac{\partial \lambda}{\partial \Lambda} \cdot \frac{\Lambda_1}{\lambda_A}\right)\right|. \tag{4.8}$$

Since $\frac{\partial \lambda}{\partial \Lambda}$ is a positive tuning function and $\lambda_A > \Lambda_1$, obviously

$$\left|\left(1 - \frac{\partial \lambda}{\partial \Lambda} \cdot \frac{\Lambda_1}{\lambda_A}\right)\right| < 1. \tag{4.9}$$

Finally we obtain the relation

$$|\delta\lambda_2| < |\delta\lambda_1|. \tag{4.10}$$

After several iterations, $\delta\lambda$ will vanish and the central wavelength will converge at $\lambda_0$.

In order to illustrate the effectiveness of the iteration method, we examine the following examples. The first example is a Bragg grating for TE polarization shown in Fig. 11. The etching depth is 0.5 μm; all the other parameters remain the same as those used in Fig. 13. To calculate the reflection spectrum of the fundamental TE mode, we

utilize the complex mode matching method, which has been validated with comparison with the bi-directional beam-propagation method as shown in Fig. 13.

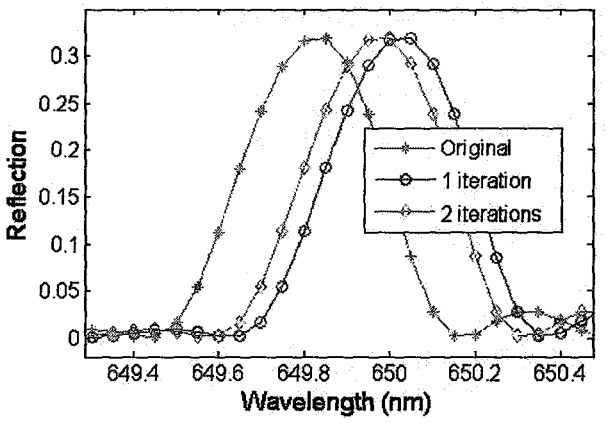


Fig. 16. Reflection spectra of the fundamental TE mode during the design. Star: original design; circle: after 1 iteration; diamond: after 2 iterations.

Fig. 16 demonstrates the reflection spectra of the fundamental TE mode during the design process. The curve marked with star is the spectrum using the original designed parameters which is under fundamental local mode calculation($\Lambda_1$= 0.106456 μm and $\Lambda_2$=0.106553 μm); the curve marked with circle represents the reflection spectrum after 1st iteration; and the curve marked with diamond is the reflection spectrum after 2nd iteration. It's noticed the shift is quite large using under fundamental mode estimation. However, the central wavelength converges to the designed central wavelength very fast using iterative method.

To illustrate the effectiveness and flexibility of the method described above for the TM polarization with high index contrast. We have used our approach to design a one-dimensional (1D) photonic crystal slab (PCS). This structure consists of alternating layers

of two different symmetric slab waveguide segments with high index contrast in transverse direction, as shown in Fig. 17.

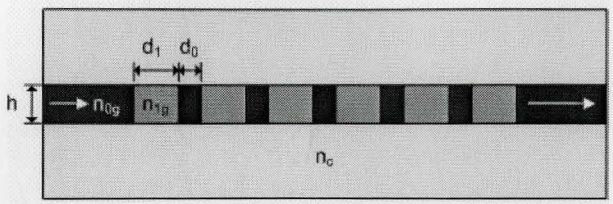


Fig. 17 . Schematic diagram of 1D photonic crystal slab waveguide (PCSW).

The two different waveguide segments have common cladding index $n_c = 1.45$, and different core indexes $n_{0g} = 3.4$ and $n_{1g} = 2.518$, respectively. The widths of the two segments are calculated under fundamental local mode calculation ($d_0 = 0.17392$ μm, $d_1 = 0.22972$ μm). The core thickness is $h = 0.25$ μm and the number of periods is 32. The designed central wavelength is 1550nm.

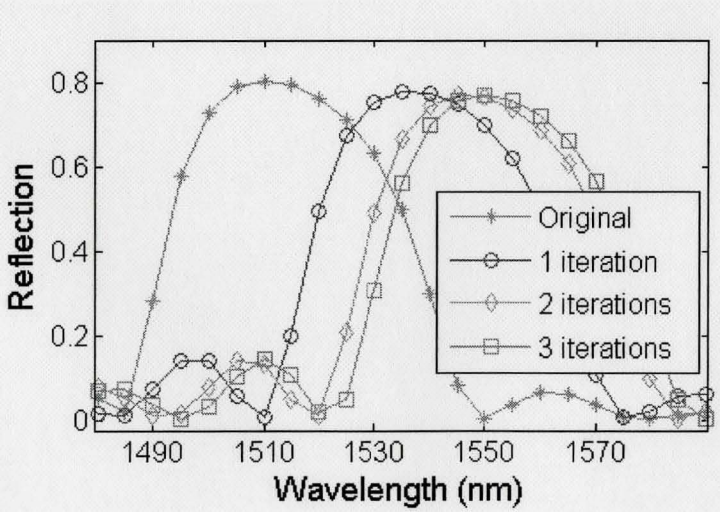

Fig. 18 .Reflection spectra of the fundamental TM mode during the design for 1D photonic crystal slab waveguide (PCSW). Star: original design; circle: after 1iteration; diamond: after 2 iterations; square: after 3 iterations.

The results in Fig. 18 demonstrate that even the original central wavelength shifts a lot from the designed wavelength ( $\Delta\lambda$ =40nm), after three iterations, the central wavelength will converge at 1550nm ( $d_0 = 0.1809$ μm, $d_1 = 0.2389$ μm).

# Chapter 5

# Simulation and Analysis of Bragg Gratings in Surface Plasmonic Polariton Waveguides

## 5.1 Introduction

Surface plasmon-polaritons (SPP) attracted much interest due to their unique properties characterized by large electromagnetic fields confined within a sub-wavelength region [2, 13-20]. It has recently been shown a thin metal film surrounded by dielectric medium can support two bound TM modes in which the symmetric mode has a very small attenuation constant, therefore the symmetric mode is often referred to as a long range surface plasmon-polariton (LR-SPP) and can be used to constitute low loss photonic components [3]. LRSPP Bragg grating has been investigated both theoretically and experimentally as a promising replacement of traditional dielectric gratings which are widely used in distributed feedback (DFB) and distributed Bragg reflector (DBR) lasers.

## 5.2 Mode Characteristics of SPP Waveguide

### 5.2.1 Mode characteristics of SPP waveguides of single interface

Fig. 19 displays the guided, quasi-leaky and PML mode of the single interface SPP waveguide with Au as the metal, and air or BCB polymer (n=1.545) as the dielectric. It's shown the guided mode decreases exponentially in the direction perpendicular to the

interface; the quasi-leaky modes grow towards the surrounded mediums while the PML modes oscillate in the PML region.

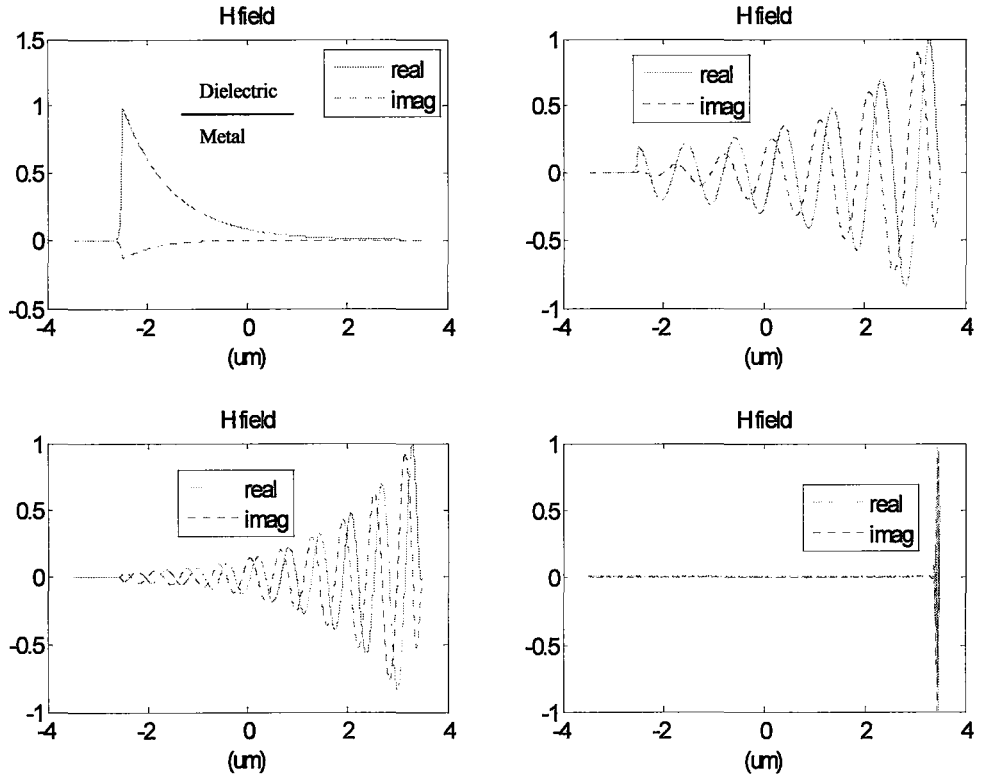


Fig. 19. Mode characteristics of SPP waveguides of single interface

### 5.2.2 Mode characteristics of SPP waveguides of double interface

Fig. 20 displays the guided, quasi-leaky and PML mode of the two-interface SPP waveguide with Au as the metal, and air or BCB polymer (n=1.545) as the dielectric. It's shown the structure supports two guided mode. One is symmetric mode, another is anti-symmetric mode. The symmetric mode has smaller imaginary part, therefore can propagate much longer than the anti-symmetric mode, therefore it is also called long

range surface plasmon polaritions (LRSPPs). The quasi-leaky modes grow towards the surrounded mediums while the PML modes oscillate in the PML region.

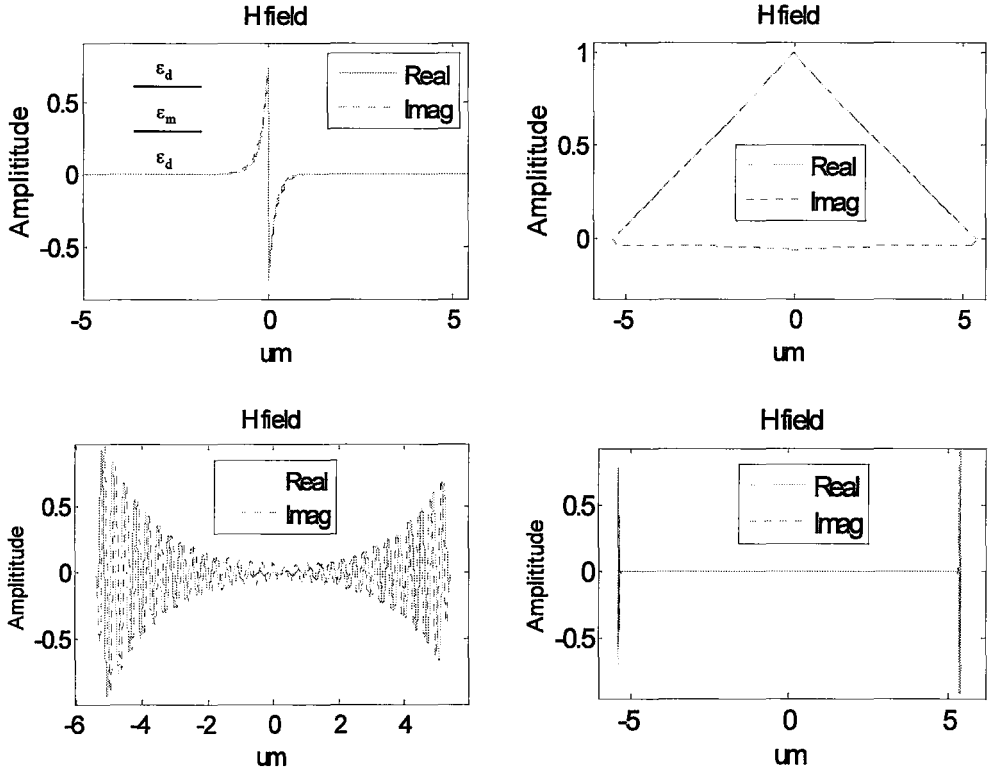


Fig. 20. Mode characteristics of SPP waveguides of single interface

### 5.2.3 Mode characteristics of SPP waveguides of MDM structures

Planar SPP waveguides may be classified into two categories according to the materials structure, dielectric-metal-dielectric (DMD) type and metal-dielectric-metal (MDM) type. The DMD structures can propagation much longer than MDM structure, whereas MDM structures have much better confinement performances. Fig. 21 displays the guided, quasi-leaky and PML mode of the MDM SPP waveguide with air or $SiO_2$ as the core, and

air or BCB polymer (n=1.545) as the metal. It's shown the field of the guided mode is squeezed in the core region.

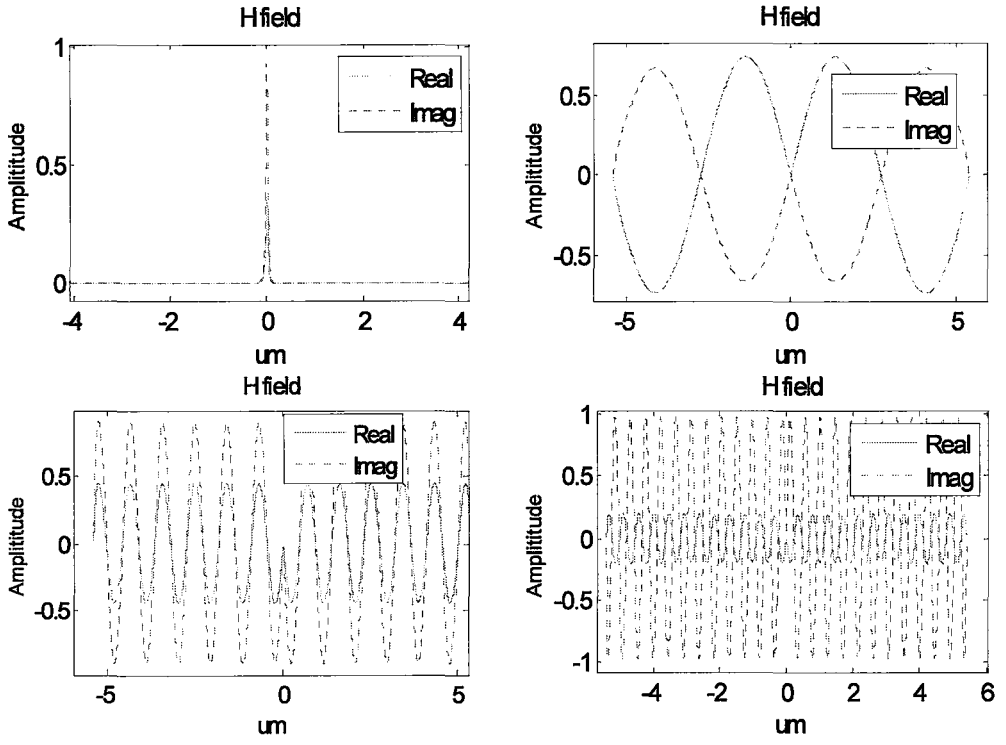


Fig. 21.Mode characteristics of SPP waveguides of MDM structure

## 5.3 Reflection, transmission and loss of a single junction

The studied structure consists of an Au film surrounded by polymer materials (BCB), the geometry is illustrated in Fig. 22. Reflection, transmission and loss are calculated at the optical frequency 1550 nm. The refractive index of Au and BCB used in calculation are ($n_{Au} = 0.559 - 9.81i$, $n_{BCB} = 1.543$).

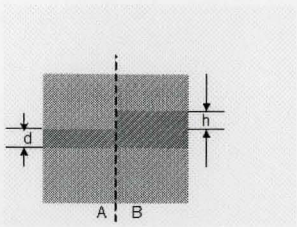


Fig. 22. Schematic of a single SPP junction

The configuration of the discontinuity considered consists of two sections (section A and section B), and on each section of the discontinuity there are two types of modes. One is symmetric mode (S-mode), another is called anti-symmetric mode (A-mode).

We analyze reflection, transmission coefficient of the S-mode and A- mode SPP at the wavelength of 1550 nm for different discontinuities using finite difference mode matching method. The numerical results are shown in Fig. 23 and Fig. 24, respectively. For the sake of accuracy, 40 modes were used in finite difference mode matching method.

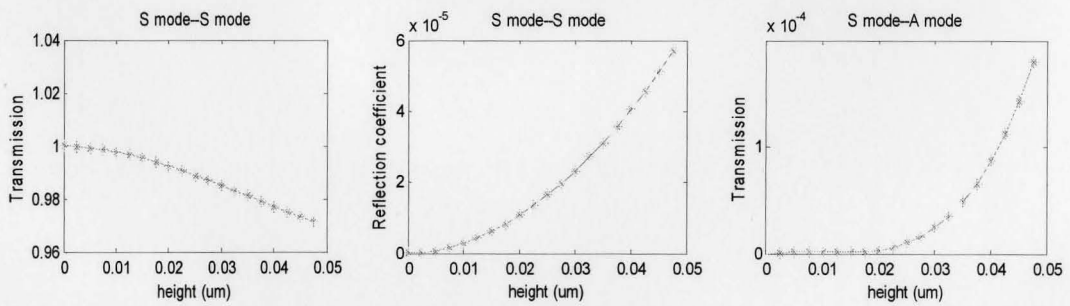


Fig. 23. Reflection, transmission of symmetric mode as a function of height at a discontinuity consists of a 15 nm Au strip surrounded by polymer. (a) transmission between S-mode in section A and S-mode in section B, (b) reflection between S-mode in section A and S-mode in section A,(c) transmission between S-mode in section A and A-mode in section B.

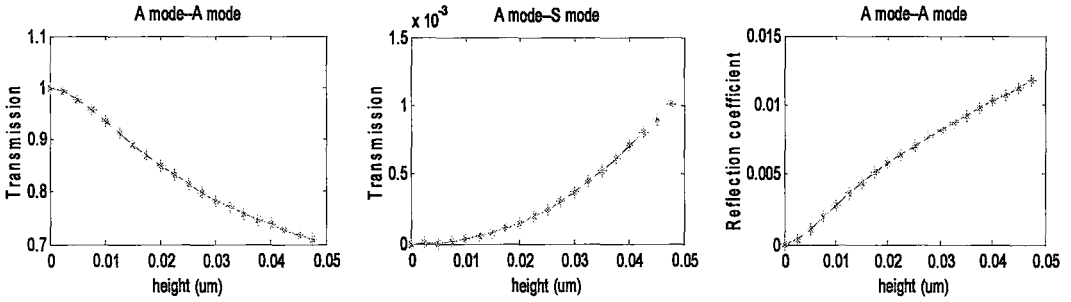


Fig. 24. Reflection, transmission of anti-symmetric mode as a function of height at a discontinuity consists of a 15 nm Au strip surrounded by polymer. (a) transmission between S-mode in section A and S-mode in section B, (b) reflection between S-mode in section A and S-mode in section A,(c) transmission between S-mode in section A and A-mode in section B.

The simulation results show that the power reflectivity of increases while transmission decreases with the thickness in both cases. It's noted the reflection of anti-symmetric mode is much larger than symmetric mode. It's also found that although the transmission of A-S mode and S-A mode increasing with height, it's still very small comparing to S-S mode transmission or A-A mode.

## 5.4 Reflection, transmission and loss of asymmetric SPP waveguide grating

The SPP grating structure can be constructed by corrugations along the metallic film surface as shown in Fig. 25. In order to make a difference with the ridge waveguide gratings discussed later, we named this kind of gratings as asymmetric grating since it only has corrugations on the single interface. The metal used in this grating is a gold film

with thickness D. The surrounded medium is polymer materials (BCB, n=1.545). Reflection, transmission and loss are calculated at the optical frequency 1550 nm. The refractive index of Au and BCB are considered invariant in a narrow range (1552-1558 nm), the parameters used in calculation are ($n_{Au}$=0.559-9.81i, $n_{BCB}$=1.543).

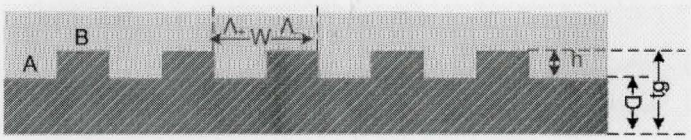


Fig. 25. Schematic of SPP grating structure consisting of a metal slab with a corrugated top surface, dielectric substrate, and polymer.

$t_g$

As the first example, we consider a thick metal structure (D→∞) for which only the top metal-dielectric interface is critical. Only one guided surface mode exists along the interface between dielectric and metal, therefore the Bragg period is fixed and not varying as a function of grating height. In this work, the duty cycle used is 50%, and the grating period at Bragg wavelength of 1550nm is calculated to be Λ=596 nm.

Assume a SPP mode is propagating along the metal from the left-hand side and incident on the grating at z=0. Part of the waves is reflected and part transmitted. Also, there will be absorption and radiation loss suffered by the wave going through the grating region. In our simulation, we have assumed total of 100 periods and the grating height H=10 nm. Fig. 26 shows the reflection, transmission and loss spectra with 1, 40, and 60 modes, respectively. It is noted that the single surface mode approximation over-estimates the loss and is subject to errors in prediction of the reflection and transmission spectra.

The simulation results converge as the number of modes exceeds 60. The overall loss predicted by the simulation based on multi-modes is significantly lower than that of

single mode approximation, indicating that there is considerable re-capture of the radiation wave by successive junctions in the Bragg gratings.

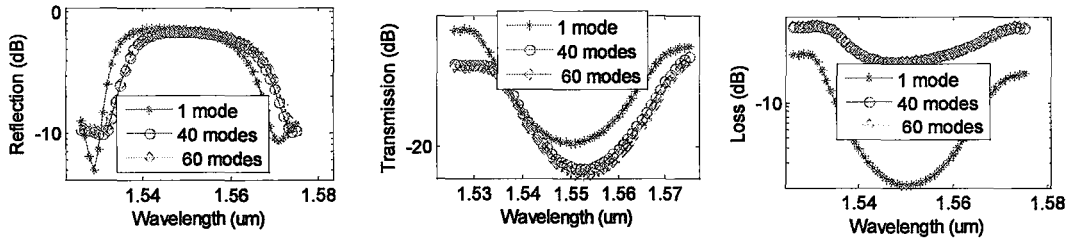


Fig. 26. Reflection, transmission and loss of a single interface SPP grating with 10 nm ridges, 100 periods. Star-1 mode, circle-40 modes, diamond: 60 modes.

We investigated the effects of grating height on the reflection, transmission and loss spectra. Fig. 27 shows the spectra for H=10, 20, 60 nm, respectively. The peak reflectivity increase as a function of H, whereas the minimum transmission and loss decrease with height, this we may explain by the fact that more power being reflected back and smaller penetration of the field into the grating region.

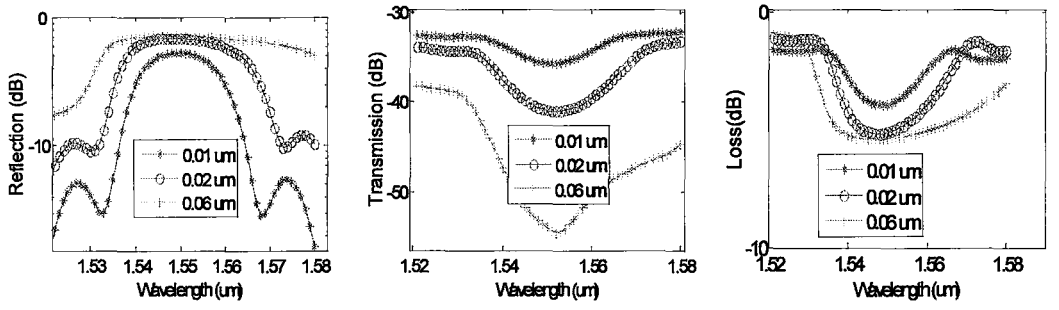


Fig. 27. Reflection, transmission and loss of a single interface grating consist of Au and polymer for different heights. Star-10 nm, circle-20 nm, plus- 60 nm.

As the thickness of the grating D is limited, for instance, for a thin metallic strip (tg equals to 35nm) which both interfaces are critical, there are two modes among which symmetric is known as the long range surface plasmon polaritons mode (LRSPPs). We investigated the reflection, transmission and loss as a function of varied height for symmetric mode (Fig. 28). It's noted the LRSPP grating is a weak grating has narrower bandwidth comparing to bulk grating, and the peak reflectivity increase as a function of h.

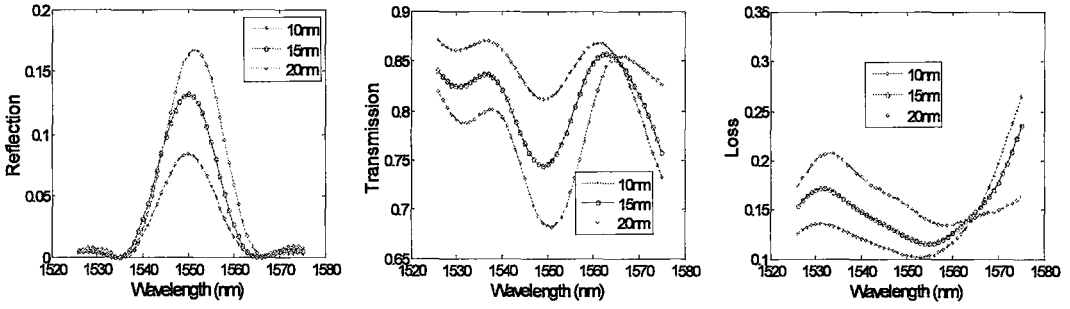


Fig. 28. Reflection (a), transmission (b), and loss (c) of the SPPs gratings with respect to different h, 100 periods. Star: h=10nm; circle: h=15nm; diamond: h=20nm.

## 5.5 Reflection, transmission and loss of ridge SPP waveguide gratings

The SPPS grating also can be constructed by the corrugations in both surfaces (Fig. 29), the LRSPPS Bragg gratings have been studied both theoretically and experimentally in [17]. The thickness of the core width is 15 nm; section length is 230nm and 270 nm, respectively. We investigated the reflection, transmission and loss as a function of h, simulation results are shown in Fig. 30.

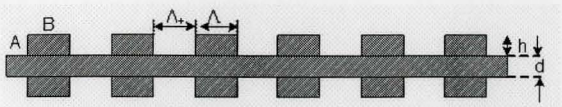


Fig. 29. Schematic of SPP ridge gratings

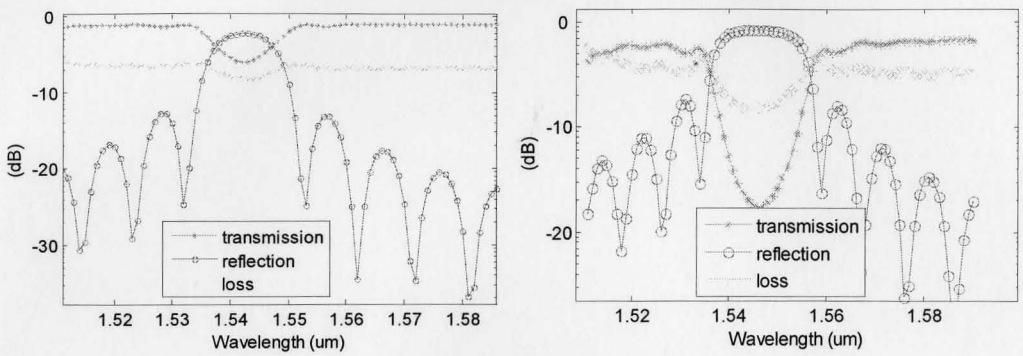


Fig. 30. Reflection and transmission spectrum for LRSPP gratings composed of a 15nm gold film with an array of gold ridges with 500 nm spacing and 230nm width, 160 ridges (a) h= 10 nm, (b) h =20 nm.

It's shown that that reflection peak and the bandwidth increases with the ridge height, and the numerical results are in good agreement with the experimental results.

## 5.6 Reflection, transmission and loss of alternate slab SPP waveguide grating

The most common ways to construct a dielectric-metal-dielectric grating is by changing the width or height of the metallic films (as discussed in the previous sections). Although it is straightforward and easy for fabrication, however, the absorption loss is increased due to the width variation, and it is noted that the grating construct in this way is a weak grating. Here we propose a new grating by alternating the surround dielectric mediums.

The metal film can be made very thin, and the coupling strength can be adjusted by the contrast of the difference of the dielectric mediums (Fig. 31).

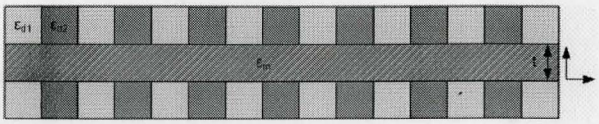

Fig. 31. Schematic of alternate slab SPP waveguide grating

We designed a DMD gratings composed of a gold film surrounded by alternate dielectric slabs, $n_{d1}$=1.46, $n_{d2}$=1.44. Fig. 32 demonstrates reflection, transmission and loss for different core width. It is shown that this structure behaves nice filtering characteristics and the loss is comparably small. It is noted the peak reflection increased with decreased core width, this may be explained by the fact that the guided field is more bounded along the interface with thinner core, therefore the field difference of the two sections is enlarged as well.

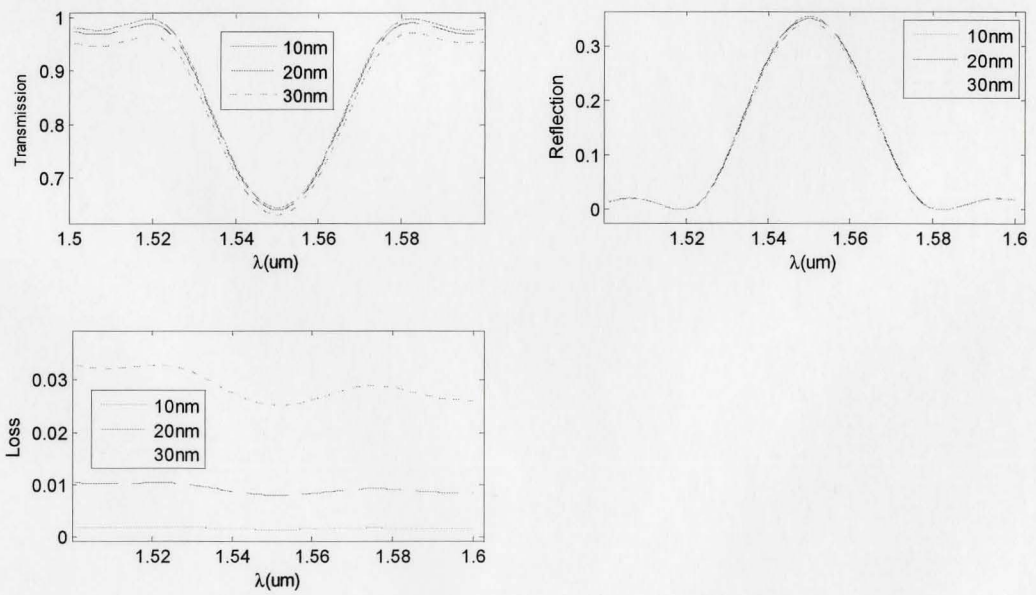

Fig. 32. Reflection and transmission spectrum a function of core thickness for DMD gratings composed of a gold film surrounded by alternate dielectric slabs, $n_{d1}$=1.46, $n_{d2}$=1.44.t=10, 20, 30nm respectively.

## 5.7 Reflection, transmission and loss of MDM SPP waveguide gratings

Although DMD structures have less loss, it has been shown that these structures exhibit bad confinement performance. On the other hand, MDM structures take the advantage of squeezing the light in a sub-wavelength scale while suffering large absorption loss. In some case when the loss can be compensated by the gain medium and confinement factor is the main concern, the MDM grating is an appropriate solution.

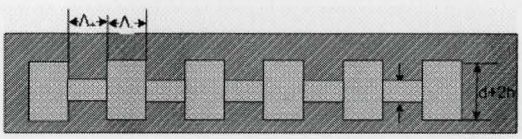


Fig. 33. Schematic of metal-dielectric-metal SPPs waveguide gratings

We design a MDM grating by periodically changing the dielectric core width (Fig. 33). The core material used is SiO2 (n=1.44), and the surrounded metal is Au. The working wavelength is 1.55 um. Fig. 34 shows the reflection and transmission spectrum as a function of core width for MDM gratings. The number of periods is 50, h=2.5nm. It is shown the peak reflection is inverse proportion to the core width.

We also investigate the effects of core materials on the grating performance, as shown in Fig. 35. The parameters used are: h=2.5nm, core width=60nm, 50 periods. It's shown the peak reflection is in proportion to the refractive index of the core materials.

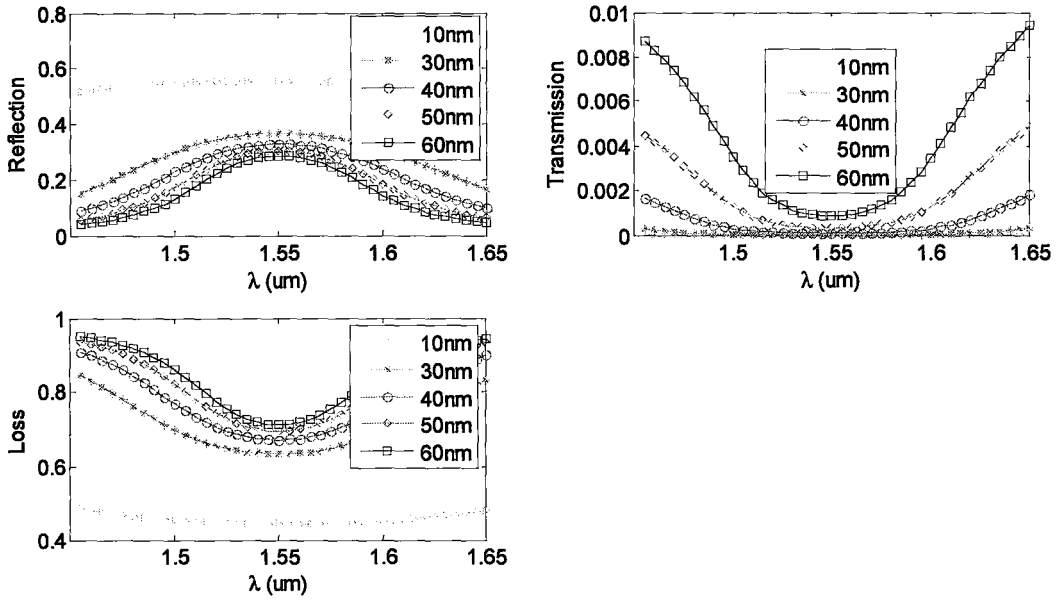


Fig. 34. Reflection and transmission spectrum for MDM gratings composed of SiO2 as core material with Au as the surrounded metal, h=2.5nm. 50 periods.

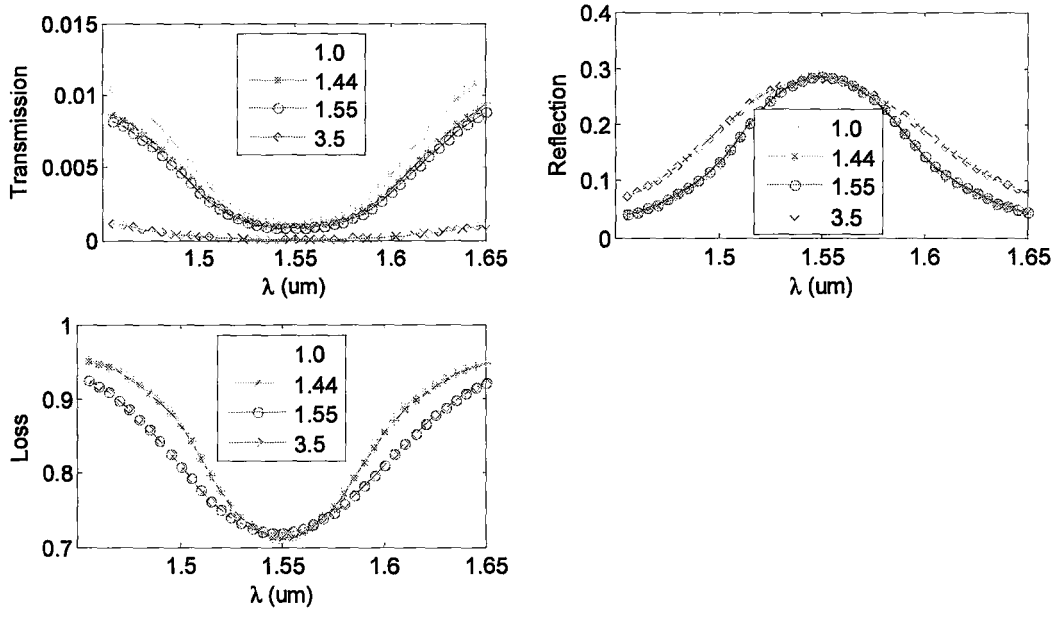


Fig. 35. Reflection and transmission spectrum as a function of core materials for MDM gratings, d=60nm,h=2.5nm. 50 periods.

Furthermore, we investigate the effects of the width difference, as shown in Fig. 36. The parameters used are: 50 periods, core width=60nm, core materials is SiO2. It's shown the peak reflection is proportional to the width difference as expected.

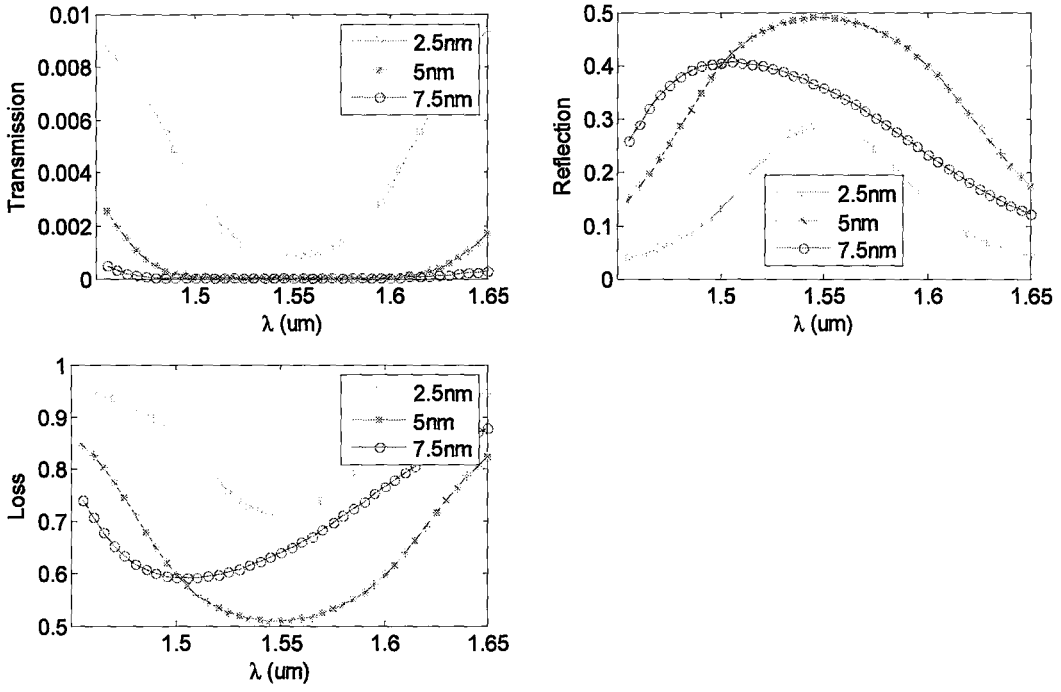


Fig. 36. Reflection and transmission spectrum as a function of h for MDM gratings composed of a gold film with SiO2 as core materials, d=60nm, 50 periods.

# Chapter 6

# Conclusions

This thesis introduces a series of techniques to model high index contrast and SPP gratings.

Waveguide Bragg grating structures with strong index corrugations and SPPs Waveguide gratings are analyzed by the complex mode-matching method facilitated by a combination of perfectly matched layer (PML) and zero boundary conditions, both surface and leaky modes of the waveguides are obtained by a fourth-order finite-difference scheme and used in the scattering matrix formulation of the mode matching method.

For Waveguide Bragg grating structures with strong index corrugations, as the index corrugation increases, the peak wavelength of the reflection spectrum is shifted towards shorter wavelength from the conventional Bragg condition due to the energy storage effect. It is shown that the peak wavelength corresponds to the center of the stop-band of the Floquet-Bloch mode and can be readily calculated by a simple iterative scheme from the conventional Bragg wavelength.

For surface plasmon polariton (SPP) grating structures, reflection, transmission and loss of the various Bragg gratings are simulated and their dependence on key waveguide and grating parameters are investigated.

# Bibliography


[1] D. Marcuse, "Theory of dielectric optical waveguides," *New York, Academic Press, Inc., 1974. 267 p.*, 1974.

[2] W. L. Barnes, A. Dereux, and T. W. Ebbesen, "Surface plasmon subwavelength optics," *Nature*, vol. 424, pp. 824-830, 2003.

[3] J. J. Burke, G. I. Stegeman, and T. Tamir, "Surface-polariton-like waves guided by thin, lossy metal films," *Physical Review B*, vol. 33, pp. 5186-5201, 1986.

[4] S. T. Peng, T. Tamir, and H. L. Bertoni, "Theory of periodic dielectric waveguides," *IEEE Trans. Microwave Theory Tech*, vol. 23, pp. 123–133, 1975.

[5] S. H. Chang, T. C. Chiu, and C. Y. Tai, "Propagation characteristics of the supermode based on two coupled semi-infinite rib plasmonic waveguides," *Optics Express*, vol. 15, pp. 1755-1761, 2007.

[6] A. Yariv and M. Nakamura, "Periodic Structures for Integrated-Optics," *IEEE Journal of Quantum Electronics*, vol. 13, pp. 233-253, 1977.

[7] C. Elachi and C. Yeh, "Frequency selective coupler for integrated optics systems," *Optics Communications*, vol. 7, pp. 201-204, 1973.

[8] M. L. Jones, R. P. Kenan, and C. M. Verber, "Rectangular Characteristic Gratings for Wave-Guide Input and Output Coupling," *Applied Optics*, vol. 34, pp. 4149-4158, 1995.

[9] W. Streifer, D. Scifres, and R. Burnham, "Coupled wave analysis of DFB and DBR lasers," *IEEE Journal of Quantum Electronics*, vol. 13, pp. 134-141, 1977.

[10] F. Yu and W. Knoll, "Surface plasmon diffraction biosensor," *Journal of Nonlinear Optical Physics & Materials*, vol. 14, pp. 149-160, 2005.

[11] A. D. Kersey, M. A. Davis, H. J. Patrick, M. LeBlanc, K. P. Koo, C. G. Askins, M. A. Putnam, and E. J. Friebele, "Fiber grating sensors," *Journal of Lightwave Technology*, vol. 15, pp. 1442-1463, 1997.

[12] R. Maaskant, T. Alavie, R. M. Measures, G. Tadros, S. H. Rizkalla, and A. GuhaThakurta, "Fiber-optic Bragg grating sensors for bridge monitoring," *Cement & Concrete Composites*, vol. 19, pp. 21-33, 1997.

[13] S. Jette-Charbonneau, R. Charbonneau, N. Lahoud, G. Mattiussi, and P. Berini, "Demonstration of Bragg gratings based on long-ranging surface plasmon polariton waveguides," *Optics Express*, vol. 13, pp. 4674-4682, 2005.

[14] S. Jette-Charbonneau, R. Charbonneau, N. Lahoud, G. A. Mattiussi, and P. Berini, "Bragg gratings based on long-range surface plasmon-polariton waveguides: Comparison of theory and experiment," *IEEE Journal of Quantum Electronics*, vol. 41, pp. 1480-1491, 2005.

[15] A. Boltasseva, S. I. Bozhevolnyi, T. Nikolajsen, and K. Leosson, "Compact Bragg gratings for long-range surface plasmon polaritons," *Journal of Lightwave Technology*, vol. 24, pp. 912-918, 2006.

[16] A. Hosseini and Y. Massoud, "A low-loss metal-insulator-metal plasmonic bragg reflector," *Optics Express*, vol. 14, pp. 11318-11323, 2006.

[17] T. Sondergaard, S. I. Bozhevolnyi, and A. Boltasseva, "Theoretical analysis of ridge gratings for long-range surface plasmon polaritons," *Physical Review B*, vol. 73, pp. -, 2006.

[18] Z. H. Han, E. Forsberg, and S. L. He, "Surface plasmon Bragg gratings formed in metal-insulator-metal waveguides," in *IEEE Photonics Technology Letters*, vol. 19, 2007, pp. 91-93.

[19] A. Taflove and S. C. Hagness, *Computational electrodynamics : the finite-difference time-domain method*, 3rd ed. Boston: Artech House, 2005.

[20] T. Sondergaard and S. I. Bozhevolnyi, "Out-of-plane scattering properties of long-range surface plasmon polariton gratings," *Physica Status Solidi B-Basic Solid State Physics*, vol. 242, pp. 3064-3069, 2005.

[21] H. Derudder, D. De Zutter, and F. Olyslager, "Analysis of waveguide discontinuities using perfectly matched layers," *Electronics Letters*, vol. 34, pp. 2138-2140, 1998.

[22] Y. P. Chiou, Y. C. Chiang, and H. C. Chang, "Improved three-point formulas considering the interface conditions in the finite-difference analysis of step-index optical devices," *Journal of Lightwave Technology*, vol. 18, pp. 243-251, 2000.

[23] S. S. A. Obayya, B. M. A. Rahman, K. T. V. Grattan, and H. A. El-Mikati, "Full vectorial finite-element-based imaginary distance beam propagation solution of complex modes in optical waveguides," *Journal of Lightwave Technology*, vol. 20, pp. 1054-1060, 2002.

[24] B. Rahman and J. Davies, "Finite-element solution of integrated optical waveguides," *Journal of Lightwave Technology*, vol. 2, pp. 682-688, 1984.

[25] U. Rogge and R. Pregla, "Method of lines for the analysis of dielectric waveguides," *Journal of Lightwave Technology*, vol. 11, pp. 2015-2020, 1993.

[26] U. Rogge and R. Pregla, "Method of lines for the analysis of strip-loaded optical waveguides," *J. Opt. Soc. Amer. B*, vol. 8, pp. 459–463, 1991.

[27] M. S. Stern, "Semivectorial Polarized H Field Solutions for Dielectric Wave-Guides with Arbitrary Index Profiles," *IEE Proceedings-J Optoelectronics*, vol. 135, pp. 333-338, 1988.

[28] M. S. Stern, "Semivectorial polarised finite difference method for opticalwaveguides with arbitrary index profiles," *IEE Proceedings-J Optoelectronics*, , vol. 135, pp. 56-63, 1988.

[29] C. Vassallo, "Interest of improved three-point formulas for finite-difference modeling of optical devices," *Journal of the Optical Society of America a-Optics Image Science and Vision*, vol. 14, pp. 3273-3284, 1997.

[30] C. Vassallo, "1993-1995 optical mode solvers," *Optical and Quantum Electronics*, vol. 29, pp. 95-114, 1997.

[31] W. E. Arnoldi, "The principle of minimized iterations in the solution of the matrix eigenvalue problem," *Q. Appl. Math*, vol. 9, pp. 17–29, 1951.

[32] J. P. Berenger, "A Perfectly Matched Layer for the Absorption of Electromagnetic-Waves," *Journal of Computational Physics*, vol. 114, pp. 185-200, 1994.

[33] W. P. Huang, C. L. Xu, W. Lui, and K. Yokoyama, "The perfectly matched layer (PML) boundary condition for the beam propagation method," *Photonics Technology Letters, IEEE*, vol. 8, pp. 649-651, 1996.

[34] H. Rogier and D. De Zutter, "Berenger and leaky modes in microstrip substrates terminated by a perfectly matched layer," *IEEE Transactions on Microwave Theory and Techniques*, vol. 49, pp. 712-715, 2001.

[35] W. C. Chew, J. M. Jin, and E. Michielssen, "Complex coordinate stretching as a generalized absorbing boundary condition," *Microwave and Optical Technology Letters*, vol. 15, pp. 363-369, 1997.

[36] J. Petracek and K. Singh, "Determination of leaky modes in planar multilayer waveguides," *IEEE,Photonics Technology Letters*, vol. 14, pp. 810-812, 2002.

[37] A. Yariv, "Coupled-mode theory for guided-wave optics," *IEEE Journal of Quantum Electronics*, vol. 9, pp. 919-933, 1973.

[38] S. M. Norton, T. Erdogan, and G. M. Morris, "Coupled-mode theory of resonant-grating filters," *Journal of the Optical Society of America a-Optics Image Science and Vision*, vol. 14, pp. 629-639, 1997.

[39] H. L. Rao, R. Scarmozzino, and R. M. Osgood, "A bidirectional beam propagation method for multiple dielectric interfaces," *IEEE Photonics Technology Letters*, vol. 11, pp. 830-832, 1999.

[40] P. L. Ho and Y. Y. Lu, "A bidirectional beam propagation method for periodic waveguides," *IEEE Photonics Technology Letters*, vol. 14, pp. 325-327, 2002.

[41] Y. Cheng, W. Lin, and Y. Fujii, "Local field analysis of bent graded-index planar waveguides," *Journal of Lightwave Technology*, vol. 8, pp. 1461-1469, 1990.

[42] J. Ctyroky, S. Helfert, and R. Pregla, "Analysis of a deep waveguide Bragg grating," *Optical and Quantum Electronics*, vol. 30, pp. 343-358, 1998.

[43] J. Ctyroky, S. Helfert, R. Pregla, P. Bienstman, R. Baets, R. De Ridder, R. Stoffer, G. Klaasse, J. Petracek, P. Lalanne, J. P. Hugonin, and R. M. De La Rue, "Bragg waveguide grating as a 1D photonic band gap structure: COST 268 modelling task," *Optical and Quantum Electronics*, vol. 34, pp. 455-470, 2002.

[44] C. Vassallo, *Optical Waveguide Concepts*: Elsevier, 1991.

[45] R. Sammut and A. W. Snyder, "Leaky Modes on a Dielectric Waveguide - Orthogonality and Excitation," *Applied Optics*, vol. 15, pp. 1040-1044, 1976.

[46] P. Bienstman, E. Six, A. Roelens, M. Vanwolleghem, and R. Baets, "Calculation of bending losses in dielectric waveguides usingeigenmode expansion and perfectly matched layers," *IEEE ,Photonics Technology Letters*, vol. 14, pp. 164-166, 2002.

[47] H. Derudder, F. Olyslager, D. De Zutter, and S. Van den Berghe, "Efficient mode-matching analysis of discontinuities in finiteplanar substrates using perfectly matched layers," *IEEE Transactions on Antennas and Propagation*, vol. 49, pp. 185-195, 2001.

# Appendix

The parameters of $f_j$ in eq. (2.34) are as follows:

$$f_0 = 1 + \frac{h^2\eta}{8} + \frac{h^4\eta^2}{384} + O\left(h^6\right)$$

$$f_1 = \frac{h}{2} + \frac{h^3\eta}{16} + \frac{h^5\eta^2}{768} + \theta\left(\frac{h}{2} + \frac{h^3\eta}{48} + \frac{h^5\eta^2}{3840}\right) + O\left(h^6\right)$$

$$f_2 = \frac{h^2}{4} + \frac{h^4\eta}{64} + \frac{h^4\eta}{192} + \theta\left(\frac{h}{4} + \frac{h^4\eta}{96}\right) + O\left(h^6\right)$$

$$f_3 = \frac{h^3}{12} + \frac{h^5\eta}{192} + \theta\left(\frac{h^3}{12} + \frac{h^5\eta}{320}\right) + O\left(h^6\right)$$

$$f_4 = \frac{h^4}{48}(1+\theta)$$

$$f_5 = \frac{h^5}{240}$$

Where

$$\theta = \begin{cases} 1 & \text{TE} \\ n_{i+1}^2 / n_i^2 & \text{TM} \end{cases}$$

and

$$\eta = k_0^2\left(n_i^2 - n_{i+1}^2\right).$$